UNIVERSIDAD DE CHILE
FACULTAD DE CIENCIAS FÍSICAS Y MATEMÁTICAS
DEPARTAMENTO DE INGENIERÍA ELÉCTRICA

DESIGN AND TEST OF A DIGITAL CORRELATOR FOR THE NIR HETERODYNE INTERFEROMETER

TESIS PARA OPTAR AL GRADO DE
MAGÍSTER EN CIENCIAS DE LA INGENIERÍA, MENCIÓN ELÉCTRICA

FELIPE ERNESTO BESSER PIMENTEL

PROFESOR GUÍA:
ERNEST ALEXANDER MICHAEL

MIEMBROS DE LA COMISIÓN:
NICOLAS ANDRES REYES GUZMAN
EDWARD WISHNOW
MICHAEL IRELAND

Este trabajo ha sido parcialmente financiado por CONICYT, a través de su fondo ALMA para el desarrollo de la astronomía, proyecto 31140025, QUIMAL, proyecto 1500010, y CATA-Basal PFB06.

SANTIAGO DE CHILE
2018

Resumen

En la actualidad se han comenzado las discusiones para el desarrollo de los observatorios astronómicos post E-ELT, telescopio de 39 m en construcción en el norte de Chile. Como parte de estas discusiones, la comunidad científica ha planteado desarrollar un interferómetro infrarrojo capaz de resolver un planeta durante su etapa de formación [1]. Bajo el supuesto que la resolución angular de un disco de acreción para un planeta de dimensiones similares al planeta tierra es de 0.1 milisegundos de arco, para observar dicho objeto se requiere un telescopio de 1.5 km de diámetro [2]. Dado que no existe factibilidad técnica ni económica para desarrollar un proyecto de esta envergadura, es posible usar técnicas de interferometría para lograr la misma resolución angular, pero utilizando telescopios de menor tamaño. Estas técnicas corresponden a la interferometría directa (Paranal) o heterodina (ALMA).

En el caso de la interferometría directa se transmiten los haces de luz desde cada telescopio hacia un edificio central, donde estos haces son combinados para obtener un patrón de interferencia.

Por otro lado, en el caso de la interferometría heterodina, la señal en cada telescopio es mezclada con una señal de referencia. Esta luz mezclada incide en un dispositivo no lineal y es convertida a una señal de frecuencias intermedia. Esta señal se puede transmitir a través de un cable coaxial a un computador central que calcula la matriz de correlación entre las señales de cada telescopio.

Cada topología tiene sus pros y contras. En el caso de la interferometría directa, el ancho de banda es mayor que en el caso heterodino, pero mantener la coherencia temporal entre todas las señales es mucho más difícil.

Para demostrar la capacidad técnica de la topología heterodina, el laboratorio de Astrofotónica y ondas Terahertz ha desarrollado un prototipo de interferómetro heterodino en la banda de telecomunicaciones de 1.5 µm [3] [4]. Con miras a expandir el sistema a 10 µm, donde se encuentra una excelente ventana de transparencia atmosférica y varias transiciones de compuestos químicos.

Esta tesis explica y desarrolla el diseño de este interferómetro heterodino, con especial énfasis en el desarrollo y prueba del correlacionador digital, sistema que debió ser especialmente diseñado para obtener las prestaciones requeridas.

Abstract

Nowadays the community has started the discussions for the post 30 m telescopes era. As part of these discussions, the community has expressed the need for an infrared interferometer capable of resolving a planet in its early stages [1]. Under the assumption that an earth-like planet would subtend 0.1 milli-arc-seconds from earth, a single-dish telescope needs to be at least 1.5 km in diameter in order to resolve it [2]. It is technically and economically impossible to build a telescope of this size, but it is possible to achieve the same angular resolution using an array of smaller telescopes as an interferometer. Interferometry is performed nowadays by the observatories Paranal, direct optical interferometry, and ALMA, heterodyne radio interferometry. These architectures have fundamental differences. For the case of direct interferometry, the light beams travel from each telescopes to a central building, where they are combined together to form an interference pattern. Instead, for heterodyne interferometry, each beam is mixed at the telescope with a reference signal. After the mixing, these signals are sent digitally through coaxial cables to a central computer, where the correlation matrix of the array is calculated. Each architecture has its pros and cons, and which is better depends on a number of factors related to a particular project.

In order to demonstrate the technical capabilities of an infrared heterodyne interferometer, the Astro-photonics laboratory at Universidad de Chile, has developed a prototype in the telecommunication band, 1.5 μm [3] [4]. This prototype points towards future expansion to 10 μm. At this wavelength, there is an excellent atmospheric window and there exists several chemical transitions that may be found in a forming planet.

This thesis describes the design of a heterodyne interferometer, with emphasis in the digital correlator built at the Astro-photonics laboratory.

To Francisca.

Acknowledgment

I want to express my gratitude to all the people who helped me to achieve this endeavor.
To my family, who is always holding my back.
To Clemente and Miguel, who helped me by taking the necessary measurements for this work.
To Nicolás, Ignacio, Roberto, Rocío, Javier, Taky, and Alfredo for showing me other points of views and ideas to improve my work.
To the Astro-photonics Laboratory, for cheering me up when everything went south.
Special thanks to Milena Galetovic, secretary of the program, for her help with the bureaucracy of the university.
Also to Ernest, Nicolas, Patricio, Ed and Michael for their guiding and advise in order to complete this work.

Contents

List of Figures

List of Tables

List of Symbols

b Baseline between two telescopes.

D Diameter of the primary mirror of a telescope.
$\Delta\Theta_{interferometer}$ Angular resolution of an interferometer.

u Fringe frequency.
$\Delta\Theta$ Fringe spacing.

a Amplitude of a signal $s(t)$.
AA Auto-correlation output from sub-aperture A.
AB, BA Cross-correlation outputs.
α Slope in an Allan variance plot.
$\Delta\Theta_{telescope}$ Angular Resolution of a Telescope.
BB Auto-correlation output from sub-aperture B.
c Speed of light.
$\Delta\nu$ Channel bandwidth of the system.
f, ν Frequency in Hertz.
f_{BW} Maximum Bandwidth frequency of the detector.
ω Frequency [rad].
h Planck's constant.
Δt, τ Integration time.
k, k_B Boltzmann's constant.
λ Wavelength.
μ Slope in an Allan standard deviation plot.
σ_A Allan Standard Deviation.
σ_A^2 Allan Variance.
P, p Power.
P_ν Power per bandwidth unit.
I_{ph} Photodiode's photocurrent.
ϕ Phase of the stellar signal.
$s(t)$ Signal function.
x_s Received signal.
t Time.
τ_s Delay-lines in the correlator.
T_Q Shot-noise temperature.
T_{rec} Receiver's temperature.
V_p Polarization voltage.
ω_{max} Detector's maximum operation frequency [rad].
x_r Reference signal.

Chapter 1

Introduction

Humankind has always played around the idea that someone or something lives in the skies. Ancient civilizations believed that gods lived in the skies, and that the star were painted by them. Through the times this believe underwent many forms and finally was replaced by knowledge. Nowadays we observe at the sky, by using technology, to unriddle the Universe's mysteries. In order to discover the answers to our multiple questions, each decade we develop new telescopes. This ambition to understand our surroundings has brought us to discover, 20 years ago, the first exoplanets. With the technology of that time the only ones found were big gas planets [5] [6]. Time has passed and the community has developed new instruments and facilities like the Very Large Telescope Interferometer (VLTI), the High Accuracy Radial velocity Planet Searcher (HARPS) and Atacama Large Millimeter and sub-millimeter Array (ALMA) which have the capability to detect rocky, earth-like exoplanets [7] [8].

The main problem with earth-like planets is the precision needed to observe them. These objects are smaller than the tip of a needle (0.7 mm) from 100 km away. In order to resolve them from their host star, large telescopes are required.
For single-dish telescopes, the angular resolution ($\Delta\Theta$) is determined by Rayleigh's equation (1.1), where D is the circular aperture diameter and λ the observed wavelength.

$$\Delta\Theta_{telescope} = 1.22\frac{\lambda}{D} \quad \text{[radians]} \tag{1.1}$$

Let's make the assumption we are trying to observe an accretion disk from a planetary system, with an angular resolution of 0.1 milli-arc-second (mas) [2] at a wavelength of 1.5 µm, using a single telescope. This telescope would have an approximate diameter of 3.8 km, which is mechanically impossible for a ground-based telescope and a major engineering effort for a space facility. The only way to overcome this problem is by breaking up this huge aperture into smaller connected telescopes. This approach is called interferometry.

Interferometry was developed for the first time by Thomas Young with his double slit experiment (Figure 1.1). He used a monochromatic light that hit a barrier with 2 slits. The out-coming pattern was projected into a screen.

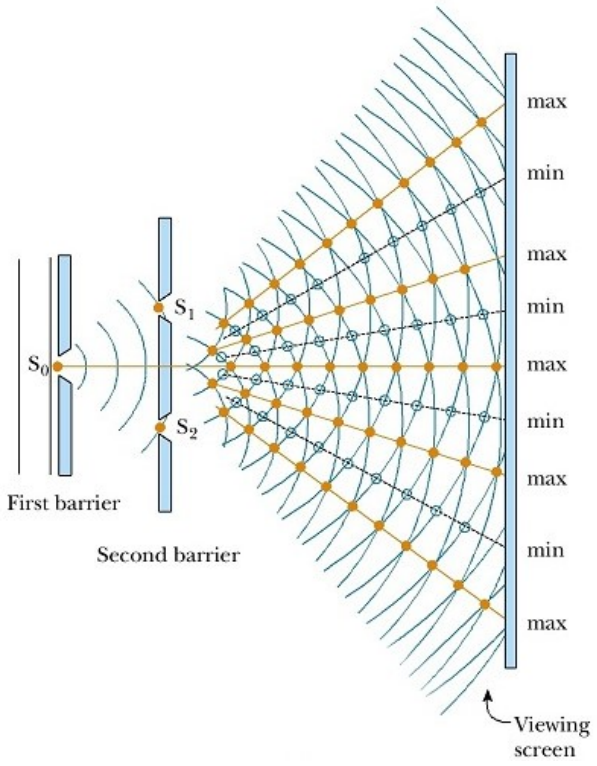

Figure 1.1: Young's double slits Experiment [9].

The fringe spacing is determined by the equation [10]:

$$\text{Fringe spacing} \equiv \Delta\Theta = \frac{\lambda}{b} \quad [\text{radians}] \tag{1.2}$$

Or, equivalently, one can regard the fringe frequency as

$$\text{Fringe frequency} \equiv u = \frac{b}{\lambda} \quad [\text{radians}]^{-1} \tag{1.3}$$

where b corresponds to the distance between the slits.

Although Young was the first to run interferometric experiments, it was Fizeau who first designed an astronomical interferometer, which was then built and tested by Michelson in 1890. With this interferometer he was able to measure the diameter of Jupiter's Moons. And with a new version, 20 feet wide, mounted on the 100 inch telescope at Mt. Wilson, California, he measured the diameter of

Betelgeuse in 1920.
In order to resolve, with this system, two different sources of incoherent light with same magnitude, the distance between the sources has to be larger than λ/2b.

$$\Delta\Theta_{interferometer} = \frac{\lambda}{2b} \quad \text{[radians]} \tag{1.4}$$

Using (1.4), it is possible to determine the baseline between two telescopes for the given angular resolution, 0.1 mas, resulting in an 1,6 km baseline interferometer.
The main difference between a large telescope and an interferometer is the smaller effective collecting area, thus longer integration time is needed to obtain the same Signal to Noise ratio (SNR). Furthermore, measurements with as many as possible baselines are needed.

There are 2 distinct ways to perform optical interferometry, one based in direct detection and the other based in heterodyne detection. In direct detection (Figure 1.2a), the light collected by each telescope is directed towards a central location, where all telescope beams are combined on an array detector, forming a fringe pattern (Figure 1.2b).
The second way to make interferometry is using heterodyne detection (Figure 1.3). In this architecture, the detection is done in each telescope by down-converting the astronomical signal with a local oscilator (LO). The resulting signal is then processed using an analog or digital correlator, getting as result the interferometric data. Interferometry architectures are explained in chapter 2.

In 2009, a near infrared (NIR) heterodyne interferometer proof-of-principle project was envisioned by Ernest Michael to be investigated in the new Astro-photonics laboratory at Universidad de Chile. The goal was to design a proof of principle interferometer using similar technologies to ALMA. This effort is inserted in the worldwide instrumental development to set ground for post 30 m class facilities.
In 2013, part of the interferometric community founded a consortium to discuss a suitable project, resulting in the Planet Formation Imager (PFI) project [1]. The Universidad de Chile heterodyne interferometer project is covered in chapter 3.

As explained previously, in a heterodyne interferometer, the combination of the data from each telescope is done by a correlator. In our case, the correlator is digital, explained in section 3.3, and the design, implementation and test was the goal of this thesis. The laboratory characterization of the system is explained and discussed in chapter 4.
Taking into consideration the goals of this thesis, it is possible to state the main hypothesis for this work as:

"It is possible to use a digital correlator to detect stellar signals at the Universidad de Chile infrared heterodyne interferometer. This correlator has to be able to compensate for long integration drift errors and reach system noise temperatures near the quantum limit".

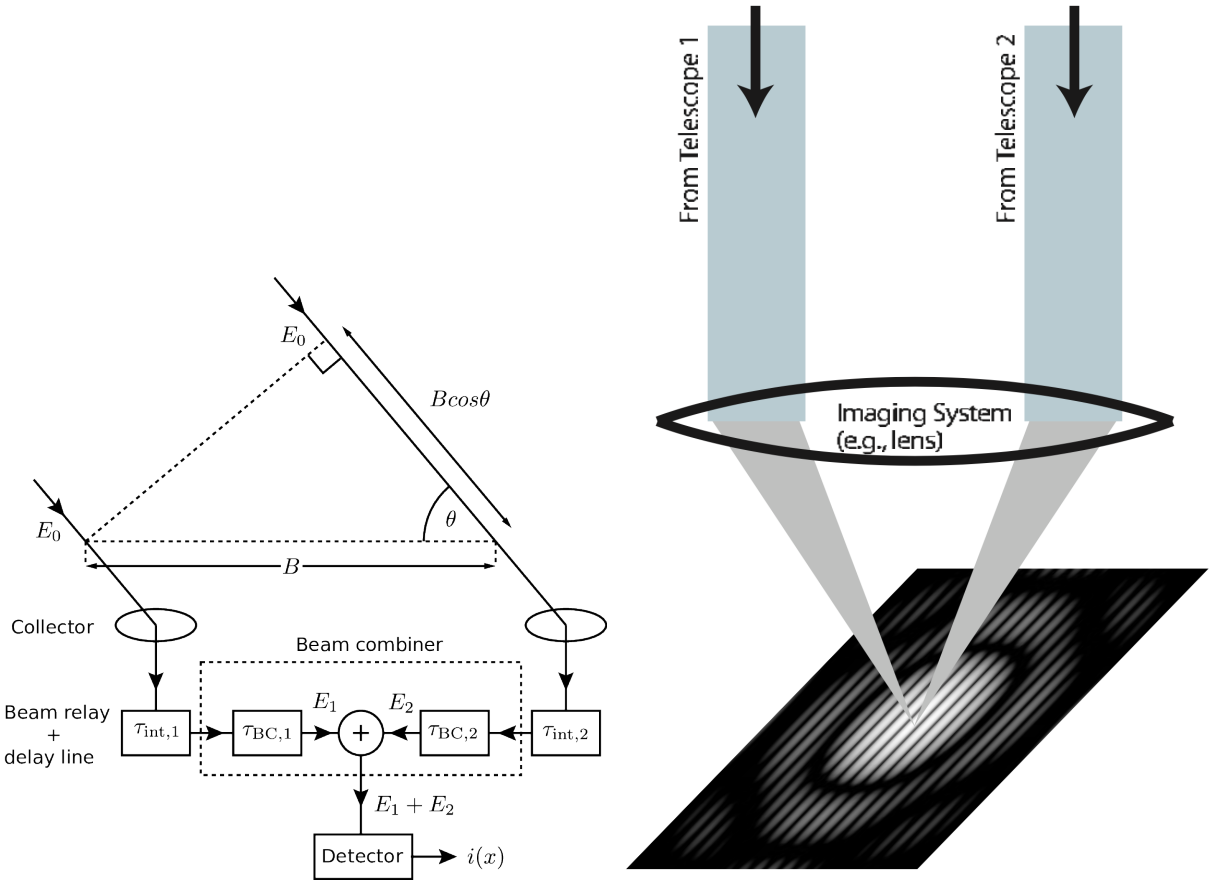

(a) Direct detection interferometer scheme [11].

(b) Interferometer pattern [12].

Figure 1.2: Direct detection interferometry.

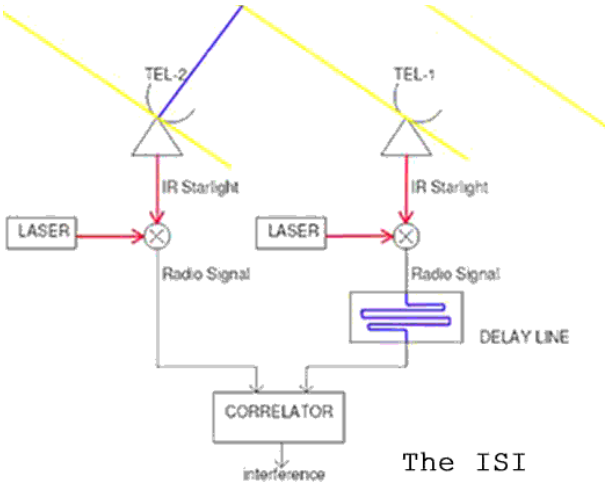

Figure 1.3: Heterodyne interferometer scheme [13].

Chapter 2

Interferometry

As explained previously, in order to peek into the apparently small objects in space, as planets under formation or the event horizon of black holes, telescope facilities need to reach the sub-mas angular resolution regime, and the only way to reach these resolutions is with interferometers even at optical wavelengths[1].

The first astronomical interferometer was constructed by Michelson in 1920 and gave the first measurement of Betelgeuse's diameter (Figure 2.1a). This interferometer used single-dish direct interferometry. Nowadays several facilities still use a similar architecture with multiple independent apertures to do interferometry. This type of interferometer is explained in section 2.1.

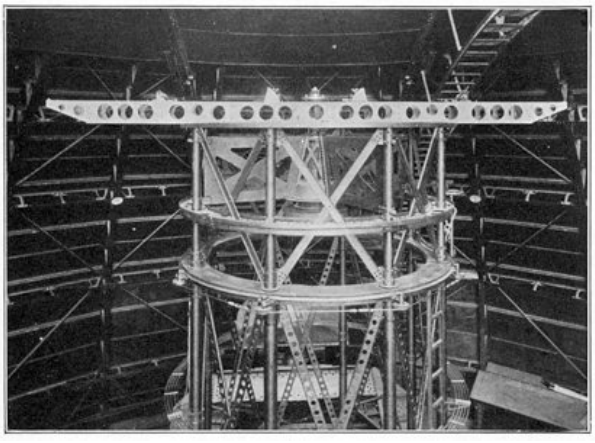

(a) Michelson Astronomical interferometer [14].

(b) Infrared Spatial Interferometer [15].

Figure 2.1: Interferometer facilities.

In 1970, Charles Townes envisioned his invention, the laser, as the central reference for an infrared "radio" interferometer (Figure 2.1b). It is strange to call IR "radio", but the idea behind it is the architecture

[1] Includes visible and infrared (IR) wavelengths

of the receiver and not the detected wavelength. In direct detection, the receiver is a CCD camera or similar (Figure 2.2a). In heterodyne detection a reference tone is mixed with the stellar signal in order to down-convert a bandwidth around the LO. This type of receivers is widely used in radio-detection, hence the name "radio interferometer" (Figure 2.2b).

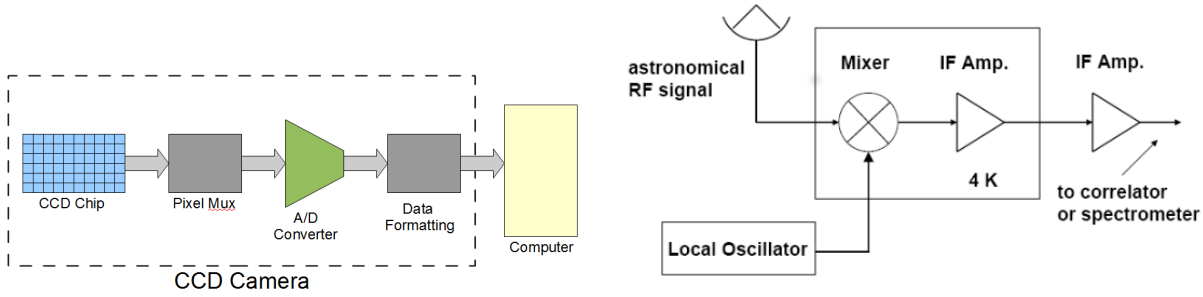

(a) Direct receiver [16].

(b) Heterodyne receiver [3].

Figure 2.2: Types of receivers used in astronomy.

Today these techniques are widely used at different optical and IR interferometers around the world. Table 2.1 presents a comparison between these projects.

Observatory	Funding	Location	N° of telescopes and diameter(m)	Baseline	Year	Wavelength (μm)	Type
GI2T	FR	Calern	2x1.5	12-65	1986	0.57-0.7	MI
ISI	USA	Mt. Wilson	3x1.65	4-70	1988	10.6	HI
COAST	UK	Cambriadge	5x0.65	48	1991	vis	MI
SUSI	AUS	Narrabi	5x0.14	5-640	1993	0.4-0.75	MI
IOTA	USA	Mt. Hopkins	3x0.45	5-38	1993	1-2.4	MI
NPOI	USA	Flagstaff	6x0.5	2-437	1994	0.45-0.85	MI
PTI	USA	Mt. Palomar	3x0.4	110	1995	2-2.4	MI
CHARA	USA	Mt. Wilson	6x1	34-331	1999	0.55-2.4	MI, FMI
KECK	USA	Mauna Kea	2x10	85	2001	2.2-10	MI
MIRA	JP	Mitaka	2x0.3	30	2001	0.8	MI
VLTI	ESO	Cerro Paranal	4x8.2 4x2.8	20-200	2001	1-12	MI
LBTI	USA	Mt. Graham	2x6.5	22.8	2005	1-20	FzI
MROI	USA	New Mexico	6x1.4	7.5-350	2008	0.6-2.4	MI

Table 2.1: Optical interferometers around the world [17].
The legend of the table is: Michelson's interferometer (MI), Heterodyne interferometer (HI), Fiber-based Michelson's interferometer (FMI) and Fizeau's interferometer (FzI).

2.1 Direct detection Interferometry

Direct detection interferometers use basically the same system designed by Michelson in 1920. This kind of interferometers, depicted in Figure 2.3, use telescopes or siderostats[2] to collect the light from the astronomical source. After that, the light-beam is relayed through tunnels to a central location for interference. As the distance traveled by the light must be the same in both arms, delay lines must be included in order to compensate the different paths. They normally consist in optics mounted on wheel carriages which can move along rails. Then, the compensated beams are lead to beam-combination and detection instruments.

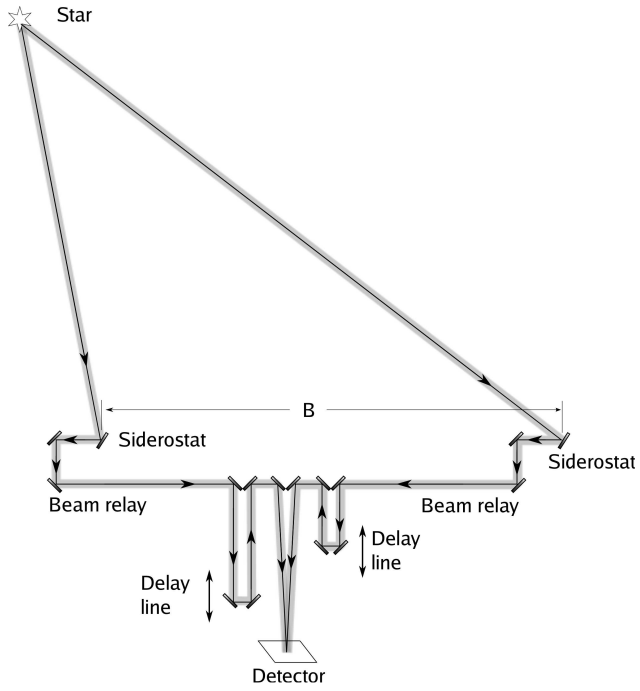

Figure 2.3: Diagram of a two aperture direct detection interferometer [11].

In order to detect an interferometric signal, two or more signals have to be received simultaneously by a single-detector. The simplest one is a square-law detector, which responds to the intensity (the square of the incident amplitude) [18].
Let us consider for simplicity in a scalar field approximation a combination of two beams ($s_1(t)$ and $s_2(t)$), which are the astronomical signals collected by each aperture. These signals are simply described by an amplitude a_i, frequency ω and phase Φ_i:

$$s_i(t) = a_i(t) \cdot \cos(\omega t + \phi_i) \tag{2.1}$$

[2]Flat mirror which redirect the light

Using a square law detector, the detected output power is defined by:

$$p(t) = [s_1(t) + s_2(t)]^2 \tag{2.2}$$

As s_1 and s_2 are complex signals, (2.2) can be rewritten as:

$$p(t) = [a_1(t)\cos(\omega t + \phi_1) + a_2(t)\cos(\omega t + \phi_2)]^2 \tag{2.3}$$

$$\begin{aligned} = & \frac{a_1^2}{2}[1 + \cos(2\omega t + 2\phi_1)] + \frac{a_2^2}{2}[1 + \cos(2\omega t + 2\phi_2)] \\ & + a_1(t)a_2(t)\ [\cos(\phi_1 - \phi_2) + \cos(2\omega t + \phi_1 + \phi_2)] \end{aligned} \tag{2.4}$$

As optical electromagnetic waves oscillate too fast for the amplitude to be directly measured, the detectors read just power of the incoming signals. Assuming a maximum frequency response of the detector(ω_{max}) smaller than ω, it is possible to rewrite (2.4) dismissing the terms with 2ωt:

$$p(t) = \frac{a_1^2 + a_2^2}{2} + a_1(t)a_2(t)\cos(\phi_1 - \phi_2) \tag{2.5}$$

Today, in multiple-telescope-interferometers, were several detectors can be used to track interference patterns from selected telescope-baselines of the array. For example, CHARA collects 6 beams, or 15 baselines, from which 7 are sampled with two CCDs [18].

2.2 Heterodyne detection Interferometry

As explained in the previous section, specifically in Figure 2.2, direct detection uses the intensity pattern from combined beams to determine the interferometric information. If no extra optics is used, the detector's output would be the intensity integral over all wavelengths, and the fringes would be washed out. In order to obtain spectroscopic information from the combined beam, a prism or other wavelength separating optics (such as a grating) has to be used in front of the detector array.
Another option to gather this information without the extra optics is heterodyne detection interferometry. In this technique, the incoming signal from each telescope is mixed with a strong monochromatic and coherent reference signal (local oscilator). The output signal, called intermediate frequency (IF) has the same phase as the original, but at lower frequencies. The process is explained in Figure 2.4, where it is possible to see the differences from direct detection interferometry (Figure 2.3). In heterodyne interferometry, the detector is placed just after a beam-splitter, which combines the signals from the telescope and LO. After this point the signals are mixed on a non-linear detector, a "mixer", and the IF signal is generated. As the IF is in the GHz band, the wavelengths for such frequencies are much larger than the optical or IR band, simplifying the construction of delay lines, amplifiers and correlators by using microwave components instead of optical.

The maximum frequency of the IF depends on the bandwidth of the electronics and detectors.

Direct detection interferometry does spectroscopy over several hundred nanometers (several THz) while heterodyne interferometers have a bandwidth of some nanometers (several GHz) [19].

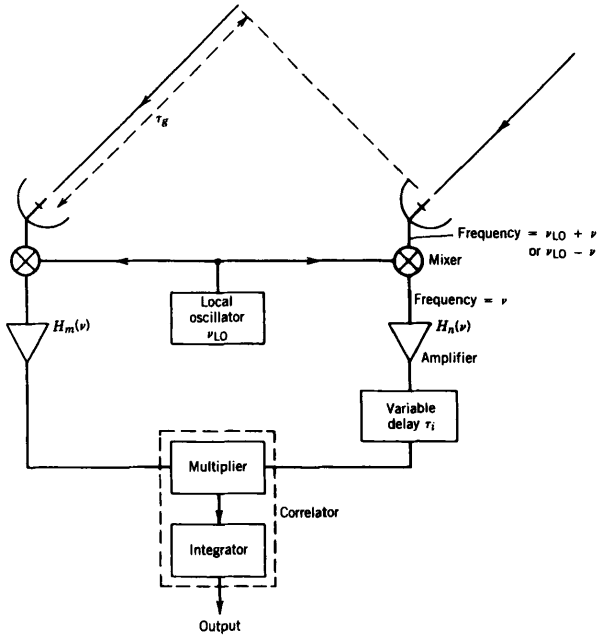

Figure 2.4: Diagram of a two aperture heterodyne interferometer [20].

Using the same square law detectors of the previous section, the math behind heterodyning is similar to direct detection. In this case the signal s_2 represents the LO, yielding (2.2) as:

$$p(t) = [a_1(t)\cos(\omega_1 t + \phi_1) + a_{lo}\cos(w_{lo}t + \phi_{lo})]^2 \tag{2.6}$$

$$= \frac{a_1^2(t)}{2}[1 + \cos(2\omega_1 t + 2\phi_1)] + \frac{a_{lo}^2}{2}[1 + \cos(2\omega_{lo}t + 2\phi_{lo})] + 2a_1 a_{lo}\cos(\omega_1 t + \phi_1)\cos(\omega_{lo} + \phi_{lo}) \tag{2.7}$$

$$= \frac{a_1^2(t)}{2}[1 + \cos(2\omega_1 t + 2\phi_1)] + \frac{a_{lo}^2}{2}[1 + \cos(2\omega_{lo}t + 2\phi_{lo})] + a_1(t)a_{lo}[\cos((\omega_1 - \omega_{lo})t + \phi_1 - \phi_{lo}) + \cos((\omega_1 + \omega_{lo})t + \phi_1 + \phi_{lo})] \tag{2.8}$$

Because the detector has a maximum IF bandwidth (f_{BW}), which is much smaller than $\omega_1/2\pi$ or $\omega_{LO}/2\pi$, it is possible to simplify (2.8) into:

$$p(t) = \frac{a_1^2(t) + a_{lo}^2}{2} + a_1(t)a_{lo}\cos((\omega_1 - \omega_{lo})t + \phi_1 - \phi_{lo}) \tag{2.9}$$

including a dc-blocking, the heterodyne signal (2.9) is expressed as,

$$p(t) = a_1(t)a_{lo}\cos((\omega_1 - \omega_{lo})t + \phi_1 - \phi_{lo}) \tag{2.10}$$

which gives information about the E-field amplitude and phase of the incoming sky signal at each telescope. A photodiode converts detected power into a photo-current ($I_{ph}(t)=R\cdot p(t)$) and the circuit converts this current into a voltage V(t). That voltage is directly proportional to the E-field before detection in front of the respective photodiode.

2.3 Correlator

By definition, the correlator is the part of the interferometer where the signals of both telescopes are "mixed" together. In direct detection, the correlator is implemented as a beam-combiner and followed by a detector, as they produce the interference signal between the telescopes. In heterodyne interferometry the correlation is done in the IF, therefore a different kind of electronics is needed to recover the interference information.

The simplest possible correlator would be a set of three electronic combiners followed by non-linear devices. Two of these combiners would mix each incoming signal with itself, and the result would be measured by an Electrical Spectrum Analyser (ESA). The last combiner would mix both incoming signals together, and the result displayed at a vectorial ESA, which collects amplitude and phase. This kind of correlator is called a XF correlator or lag correlator, as the multiplication of the channels is done prior to the Fast Furier transform (FFT), which is explained in subsection 2.3.1. The VLA and the ISI analog correlator are facilities that use this type of correlator. Another architecture performs the FFT before the mixing. This architecture is used by VLBI and ALMA-ACA [21], it is named FX-correlator and will be explained in subsection 2.3.2. The ALMA large array correlator uses a FXF correlator, where the first F correspond to a filter in order to multiplex the incoming IF spectrum into smaller chunks.

The correlation is expressed by a NxN matrix, where N is the number of sub-apertures in the array. In (2.11) a two sub-aperture correlation matrix is shown, where AA and BB correspond to the auto-correlation outputs. AB and BA correspond to the cross-correlation outputs.

$$\begin{bmatrix} AA^* & AB^* \\ BA^* & BB^* \end{bmatrix} \tag{2.11}$$

When implementing a digital correlator, an important element to take into account is the bandwidth of the system. Since multiplication in a XF correlator and the FFT in a FX correlator are computationally intensive, correlators use filter-banks before the correlation. Using this approach it is possible to split the IF bandwidth into smaller chunks, parallelizing the process. The goal behind this is to relax the requirements on the time preision of the digital correlator. A detailed and deeper explanation is found in chapter 8 of Thomson's book [20].

2.3.1 XF Correlator

As correlation is a multiplication process, in an XF correlator this correlation is done by delaying one signal with respect to the other. To obtain the cross-correlation values for the correlation matrix (2.11), a 2-branch correlator has to be implemented. A simple XF cross-correlator is depicted in Figure 2.5. To calculate the whole correlation matrix, a second correlator XF correlator needs to be added. This second block would have its inputs ,$\hat{x}$ and $\hat{y}$, detached. Using the same signal as zero delay and delayed input at the correlator, therefore obtaining the auto-correlation.
In this type of correlator, the computational power is proportional to the number of baselines of the array $\sim \frac{1}{2}N\,(N-1)$.

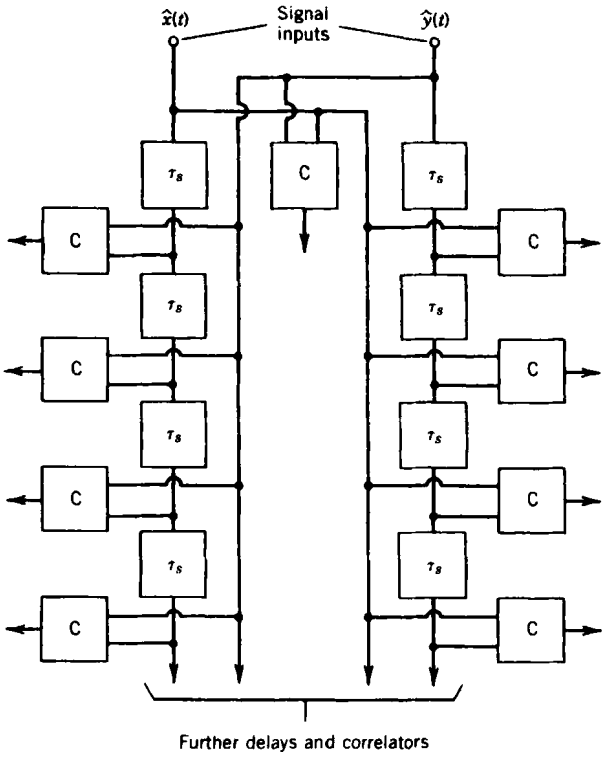

Figure 2.5: Diagram of a XF correlator [20]. Where $\hat{x}$ and $\hat{y}$ are the signal inputs, τ_s is the delay time and C corresponds to a multiplication.

2.3.2 FX Correlator

As indicated by its name, in an FX correlator the Fourier transform is performed prior to the correlation (Figure 2.6). In this case the multiplication is done in the frequency domain, consequently the correlation is as simple as multiplying the output signals of the FFT. In order to perform a correct correlation the signals have to be time-synced, as a consequence the system needs to perform a real time FFT and after that, the complex values for each antenna have to be multiplied for every frequency in the band [20].

In this type of correlator, the computational load is taken by the real FFT, and the power needed is proportional to the number of telescopes $\sim N$.

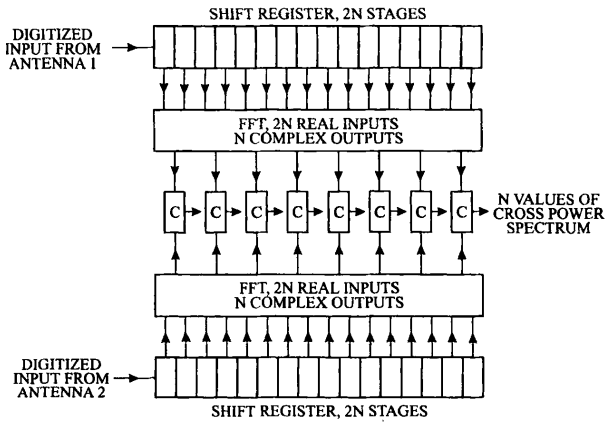

Figure 2.6: Diagram of a FX correlator [20]. Where C corresponds to a multiplication.

2.4 Detection Noise

Everything discussed till now works flawlessly in the realm of ideas. But in the real world we need to live with noise, which smears out the results. Noise has different origins, e.g: The atmosphere (changing the wavefront of the stellar signal), quantum noise from the laser, electronic noise from the thermal radiation and discretization noise in the Analog to Digital Converter (ADC), to name some. As most of these noise types are similar in both types of interferometers, I will focus the discussion to detection noise.
Several authors [22] [23] [24] [25], state that the SNR of a heterodyne double side band receiver, for a power per bandwidth unit P_ν, signal frequency ν, integration time Δt, frequency bandwidth $\Delta\nu$, 100% quantum efficiency in the detector and h being the Planck's constant, is given by (2.12). Hence, the biggest sensitivity limit for a heterodyne detector is the frequency bandwidth of the system.

$$\left(\frac{S}{N}\right)_{het} = \frac{P_\nu}{h\nu}\sqrt{\Delta\nu\Delta t} \tag{2.12}$$

For the case of an ideal detector in direct detection interferometry, with a fractional transmission of radiation reaching the telescope ε, temperature T and Boltzmann's constant k, the SNR is defined as (2.13).

$$\left(\frac{S}{N}\right)_{DD} = \frac{P_\nu}{h\nu}\sqrt{\frac{2\Delta\nu\Delta t\left(e^{h\nu/kT}-1\right)}{1-\epsilon}} \tag{2.13}$$

Both SNRs are derived in [22].

2.4.1 Receiver noise temperature

The signals detected by a heterodyne receiver have small bandwidth compared to it's central frequency, thus they can be normally considered as noise. The biggest problem is to design a receiver capable of detecting these signals and distinguish them apart from the noise generated by the receiver. Normally in radio-astronomy this receiver noise is described as a temperature (T_{rec}) and the fluctuations of this signal are defined by the radiometer equation (2.14) [31].

$$\Delta T_{rec} = \frac{T_{rec}}{\sqrt{\Delta f \tau}} \tag{2.14}$$

In theory, a single-sideband receiver temperature is determined by the shot-noise (2.15), and half shot-noise for a double- sideband receiver (2.16).

$$T_{rec,\ ssb} = \frac{h\nu}{k_B} \tag{2.15}$$

$$T_{rec,\ dsb} = \frac{1}{2}\frac{h\nu}{k_B} \tag{2.16}$$

In reality, other noises add extra temperature to T_{rec}, therefore a Y-factor method can be applied to measure the receiver temperature. This method consists on measuring the receiver output powers (P_{hot} and P_{cold}) with two different noise sources (T_{hot} and T_{cold}) and through (2.17) relate their temperatures and output powers with T_{rec}.

$$T_{rec} = \frac{T_{hot} - Y \cdot T_{cold}}{Y - 1} \qquad \text{where } Y = \frac{P_{hot}}{P_{cold}} \tag{2.17}$$

Assuming the Rayleigh-Jeans approximation, the radiation temperature of a single channel is proportional to the channel source power (2.18).

$$T_i = \frac{P_i}{k_B \Delta \nu_i} \tag{2.18}$$

By considering the thermal background at λ=1.55 μm as practically zero, and defining Y=2 in order to have a SNR=3 dB we rewrite (2.17) as (2.19).

$$T_{rec} = \frac{P_{hot}}{k_B \cdot \Delta \nu_{hot}} \tag{2.19}$$

2.5 Allan plot

The Allan variance ($\sigma_A{}^2$) and standard deviation (σ_A), as a function of an integration time τ, were introduced by D. Allan as a way to characterize the noise and stability of frequency standards. [32]. This method allows to see the impact of different noise types on the stability of the system as a log-log plot. This plot has the integration time in the x-axis and σ_A in the y-axis (Figure 2.7).
As the noises can be expressed as a simple power law for the spectral power density (2.20) [33] [34],

it is possible to determine which type of noise is influencing the system for a certain integration time, according to the slope of the plot (μ). These slopes are shown in Table 2.2 for white, flicker, random walk and frequency drift noise.

$$S(f) \sim f^{\alpha} \tag{2.20}$$

Noise	α	μ
WN PM	2	-2
FN PM	1	∼ -2
WN FM	0	-1
FN FM	-1	0
RWN FM	-2	1
Frequency drifts	-3	2

Table 2.2: Sigma-tau slopes for different types of noise [35]. White noise (WN), Flicker noise (FN), Random walk noise (RWN), Phase modulation (PM) and Frequency modulation (FM).

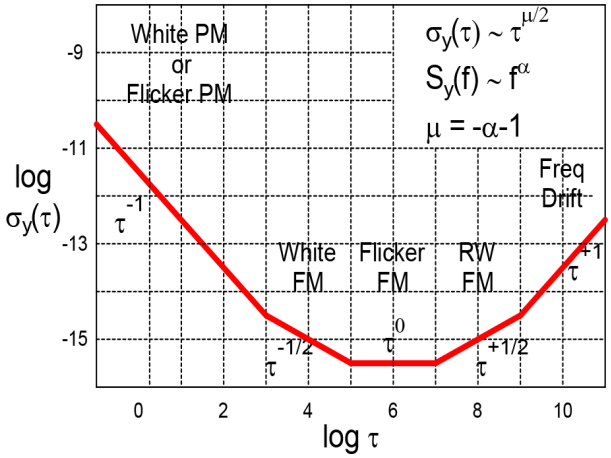

Figure 2.7: Typical profile of a sigma-tau diagram [35].

2.5.1 Allan variance for astronomical instruments

Due to the weakness of an astronomical signal, it needs to be integrated over a time τ as long as possible. In the case of heterodyne receivers, the received signal (x_s) is compared to a reference signal (x_r), in order to subtract the drift noise. As these signals are measured one after the other to ensure unchanged system behavior, it is possible to define the temporal averages of the these measurements as (2.21) and

(2.22), where $r(t)$ is the system's instantaneous output.

$$x_s(\tau,t) = \frac{1}{\tau}\int_t^{t+\tau} r(t')dt' \tag{2.21}$$

$$x_r(\tau,t) = \frac{1}{\tau}\int_{t+\tau}^{t+2\tau} r(t')dt' \tag{2.22}$$

Normally, the integration time τ is fixed, thus the output data is discrete, and the death time between integration is assumed as negligible. This way, x_s and x_r can be expressed as a summation, where k and n are the discretization of t and τ, so (2.21) and (2.22) are discretized,for Δt«τ, as:

$$\widetilde{x}_s(k,n) = \frac{\Delta t}{\tau}\sum_{i=k}^{n+k} r(i) \tag{2.23}$$

$$\widetilde{x}_r(k,n) = \frac{\Delta t}{\tau}\sum_{i=k+n+1}^{n+2k} r(i) \tag{2.24}$$

Let's define now the differences between "on" and "off" measurements as (2.25), thus obtaining the real output of the system.

$$d(\tau,t) = x_s(\tau,t) - x_r(\tau,t) \tag{2.25}$$

Or discretized (2.26).

$$\widetilde{d}(k,n) = \widetilde{x}_s(k,n) - \widetilde{x}_r(k,n) \tag{2.26}$$

From [34] it is possible to define N points-datasets for larger integration times by adding m adjacent samples using (2.27).

$$R_n(m) = \frac{1}{m}\sum_{l=1}^{k} \widetilde{d}(nm+l,n) \quad n = 0,1,\ldots,M; M = \left\lfloor \frac{N}{m} \right\rfloor - 1 \tag{2.27}$$

And so the Allan variance is defined as (2.28).

$$\sigma_A^2(m) = \frac{1}{2}\sum_{n=1}^{M} \left(R_{n+1}(m) - R_n(m)\right)^2 \tag{2.28}$$

Chapter 3

Near Infrared Heterodyne Interferometer

For the past 6 years, the Astro-photonics Laboratory has conceptualized a two-telescope prototype heterodyne interferometer for 1.55 µm [3] [36], which is based on near to shot-noise laser heterodyne detection using balanced photodiodes. The system, depicted in Figure 3.1, uses a high-coherence length laser as reference, distributed to each telescope unit (section 3.2, by the LO Distribution Box (section 3.1). At the telescope the reference signal is mixed together with the incoming sky-signal and the resulting IF signal is processed by the correlator (section 3.3). As this project has been running for years, Table 3.1 brakes down the work of our group throughout the years.

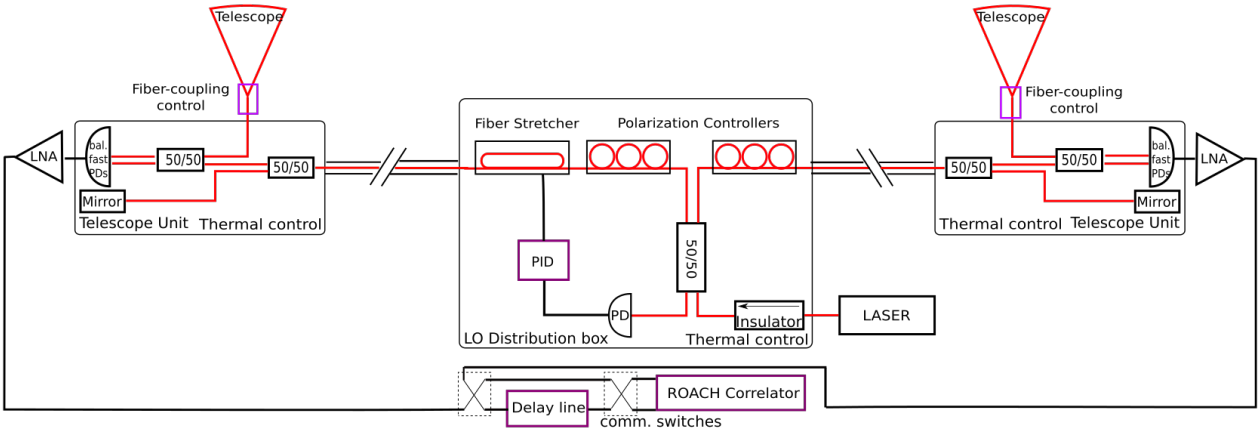

Figure 3.1: Near Infrared Heterodyne Interferometer Diagram.

2012	Laurant Pallanca	Early coupling and fiber test
	Pedro Sanchez	First correlator tests
2013	Felipe Besser	Static coupling design and tests
	Clemente Pollarolo	LO distribution and receivers design and tests
	Rodolfo Prado	
2014	Felipe Besser	Static coupling design and tests
	Clemente Pollarolo	LO distribution and receivers design and tests
	Roberto Fuentes	Correlator designs and tests
2015	Alfredo Rates	Static coupling design and tests
	Nicolás Ortega	
	Felipe Besser	Correlator designs an tests
	Roberto Fuentes	
	Felipe Besser	LO distribution and receivers design and tests
	Clemente Pollarolo	
	Miguel Piña	
2016 & 2017	Nicolás Ramos	Dynamic coupling design and tests
	Alfredo Rates	
	Nicolás Ortega	
	Sebastían Sepulveda	
	Felipe Besser	Correlator designs an tests
		Adaptive Optics preliminary designs and tests
	Clemente Pollarolo	LO distribution and receivers design and tests
	Miguel Piña	

Table 3.1: People involved in the project throughout the years.

3.1 LO Distribution Box

The distribution assembly, central box in Figure 3.1 and depicted in Figure 3.2, uses fiber optic elements to split up the master-laser into the telescopes. It consists of an optical isolator, 50/50 splitter, manual polarization controllers and the phase stabilization system. To avoid the recombination of reflections from both fiber arms in the laser, thus creating an unwanted external standing wave resonator, an optical isolator is inserted in the laser port of the beam-splitter, although the laser itself already has one internally integrated. The 4^{th} port of the 50/50 splitter is used to recombine the reflecting light from mirrors at the telescope receiver units to produce interference reference fringes for the phase stabilization system.

The phase stabilization system was inspired by ALMAs backend-photonics, where the beating between ultra-high frequency-stability and high-coherence length LO lasers, the master-laser and a slave-laser, are distributed to the telescopes with high phase-stability (40 fs), distributing a time-reference of a presition within 1.5% of the oscillation period at its highest frequency (950 GHz). To stabilize this reference signal,

ALMA uses a line-length correction (LLC) system on each individual telescope fiber connection, actively controlling the phase between the patch panel room and each antenna. The fiber-section between the lasers and the LLCs are passively stabilized by a constant-temperature environment in the patch-panel room. This passive stabilization causes long-term-drifts between the telescope phases, which are periodically corrected through phase calibrations each 900 s of observation.

The phase stabilization system designed for the NIR heterodyne interferometer, a fiber-based Michelson interferometer with a photodiode (PD) and a Proportional Integrator and Derivative (PID) actuated fiber-stretcher, stabilizes to a defined intensity level on the PD one side of the fringe, thus stabilizes the phase difference between the two end-mirrors of the fiber arms. It consists of a slow PD, a PID controller and the fiber-stretcher. The slow photodiode detects the interference fringes between the LO signal reflected by the mirrors at each telescope, giving an electrical signal between 0-5 V. This signal is fed into the PID controller, which generates a voltage for the fiber stretcher to compensate the path length of the fiber in one arm relative to the other arm, compensating the Optical path difference (OPD) between the two receiver balanced PDs.

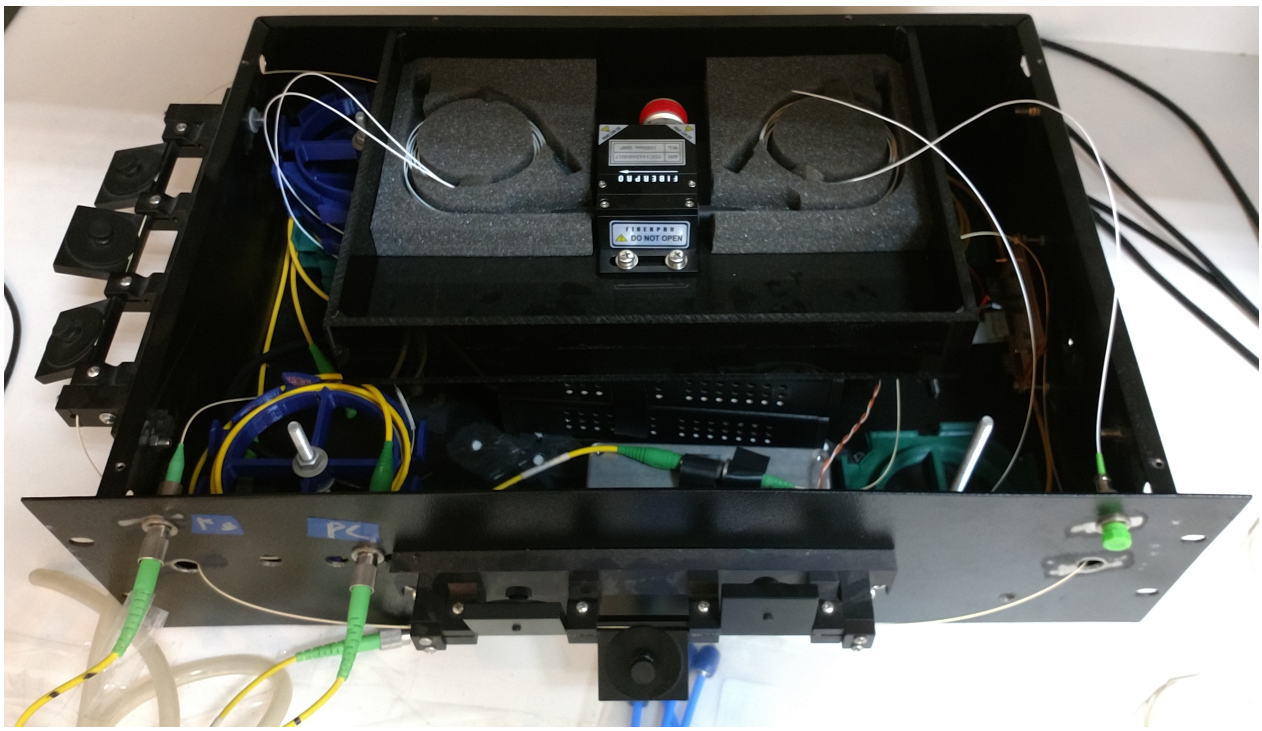

Figure 3.2: LO distribution box.
First plane has the beam-splitter. Under the beam-splitter is the LLC, vents in the middle of the picture. The gray aluminum box in the bottom of the picture is the slow photodiode for the phase stabilization. The manual polarization controllers are mounted on the outside of the box.

3.2 Coupling system and telescope unit

One of the main difficulties in astronomical instrumentation is to couple as many photons as possible from the telescope into a fiber. For interferometry sinlge-mode (SM) fiber coupling is needed in order to achieve clean interference between the telescopes. Preserving not only the intensities, but also the signal phases. A voice-coil based actuator taken from a CD-drive was used to move a ferrule-ended fiber in the focal plane as fast as possible, counteracting tip-tilt perturbations in the incoming wavefront. As the envisioned system uses small telescopes, a more complex Adaptive Optics (AO) system is probably not necessary. For larger telescopes with AO systems, this actuator could be used to "snap-in" into the existing AO-stabilized focus, which probably will have vibrational perturbations due to the telescope itself. To detect the instantaneous perturbed position of the star, the visible sky signal is transmitted trough a dichroic mirror to a Si-based quad-photodiode [3]. This signal is processed by a PID electronics and gives a correction signal to the fiber positioner, stabilizing the coupled light-level to a maximum. The NIR sky signal (at 1550 nm) is reflected by the coating of the dichroic mirror, without beam distortions, towards the SM-fiber mounted on the actuator. This coupled signal will then be detected by a balanced photodiode, which minimize the common noise of the LO.

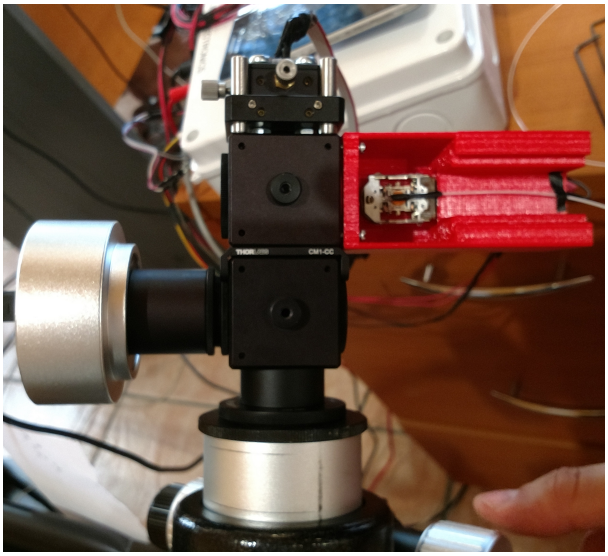

Figure 3.3: Fiber coupler assembly.
Both cubes have a dichroic beam-splitter, the bottom one has a cut-off frequency of 550 nm and the upper one has a cut-off frequency of 1100 nm. In the left side of the picture is the auto-guiding camera, in the upper side the quad-photodiode, and to the right the fiber positioner.

The balanced-diode scheme (Figure 3.4a) operates by introducing two common input signals into each photodiode. As the photodiodes are polarized in differential mode ($\pm V_p$), by reading the virtual ground between the two of them, RF Out output in Figure 3.4a, it is possible to obtain the difference between both diodes, effectively rejecting the common modes of both diodes. For this project, the 1617-AC New Focus diodes were selected (Figure 3.4b) which have an 800 MHz bandwidth, wavelength range between 900-1700 nm, and common-mode rejection of 25 dB. After the detection, the IF-signal is amplified

roughly by 60 dB and directed through coaxial cables to the ADCs of the correlator.

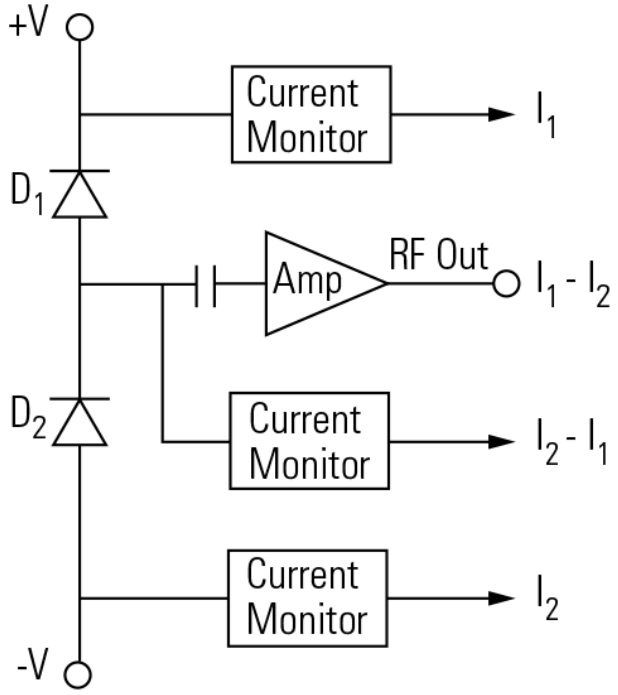

(a) Typical architecture [37].

(b) New Focus balanced photodiodes.

Figure 3.4: Balanced photodiodes.

3.3 Correlator

Since the beginning of the project, the correlator was programmed to maximize IF bandwidth, as single fast-PD were used. After some discussion in 2015, including the replacement of 5 GHz bandwidth single photodiodes for 800 MHz bandwidth balanced ones, a new scheme of correlator had to be compiled. This new scheme added a chopper to the system, and therefore the integration blocks on the correlator had to be redesigned. To design this new correlator model, a set of minimum requirements were defined. For example: Correlator bandwidth, spectral channels, bit-size of each channel etc. Throughout the work of this thesis, these requirements evolved as the architecture and components changed. The final list of requirements is presented in table 3.2.

Parameter	Ideal	Achieved
Bandwidth	800 MHz	800 MHz
Channels	As many as possible	256
Bit-size	As many as possible	18 bit from FFT
Chopper	1 Hz	8 Hz

Table 3.2: Interferometer Requirements.

Instead of an analog correlator, a digital correlator was implemented using a Reconfigurable Open Architecture Computing Hardware (ROACH) I board (Figure 3.5a) and two Texas Instrument ADCs, model ADC083000, with 8 bit digitization and 3 Giga samples per second (Gsps) (Figure 3.5b)
The basis of the designed model is an FX correlator from Collaboration for Astronomy Signal Processing and Electronics Research (CASPER) named pocket correlator. From there, extra elements were integrated in order to comply with the requirements. This extra programing could be separated into two routines, defined after the location on the correlator's model (Figure 3.6); the chopper subsystem and the integration and memory allocation.

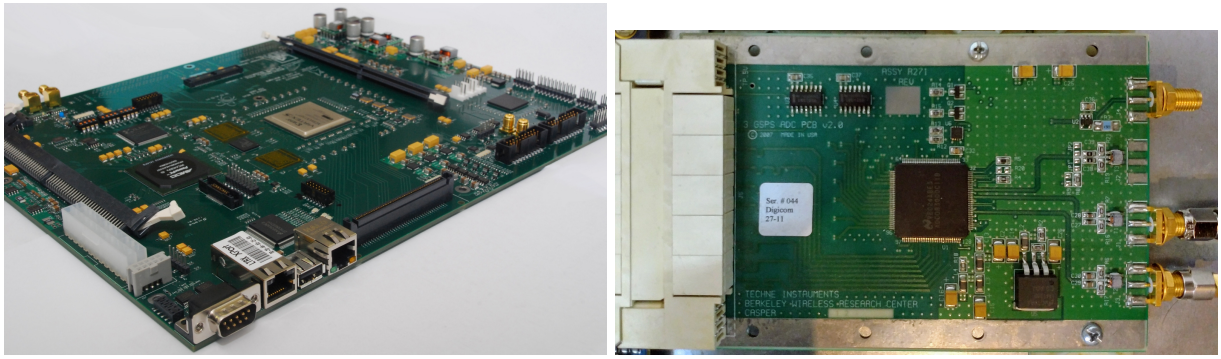

(a) ROACH board [38]. (b) ROACH ADC.

Figure 3.5: ROACH board and ADC.

3.3.1 Chopper

One way to improve a telescope's performance is through a chopper. This element allows a receiver to be compared against a known reference source (load), which is used to subtract partially the system's drift noise, improving the sensitivity of the correlator. The output signal from the correlator is going to alternate between the in sky ("on") measurement and reference ("off") measurement. Therefore the chopper has to synchronize the integration sub-system of the correlator to obtain an exact on-off measurement.
The ROACH system includes a series of General Purpose Input/Output (GPIO) pins to control or interact with the Field Programmable Gate Array (FPGA) chip. Four of these gates have a Sub-miniature A (SMA) connector. Two are for low speed I/O, and the other two are 500 MHz clock comparators [39]. One of the later was connected to the clock output of the chopper.
As the chopper controls the integration reset of the memory blocks, which are at the end of the correlator model (Figure 3.7a), a delay had to be inserted in order to reset the memory at the precise moment. This feature was implemented through a digital revision of data-paths, determining the precise amount of delay needed, depicted in Figure 3.7b.

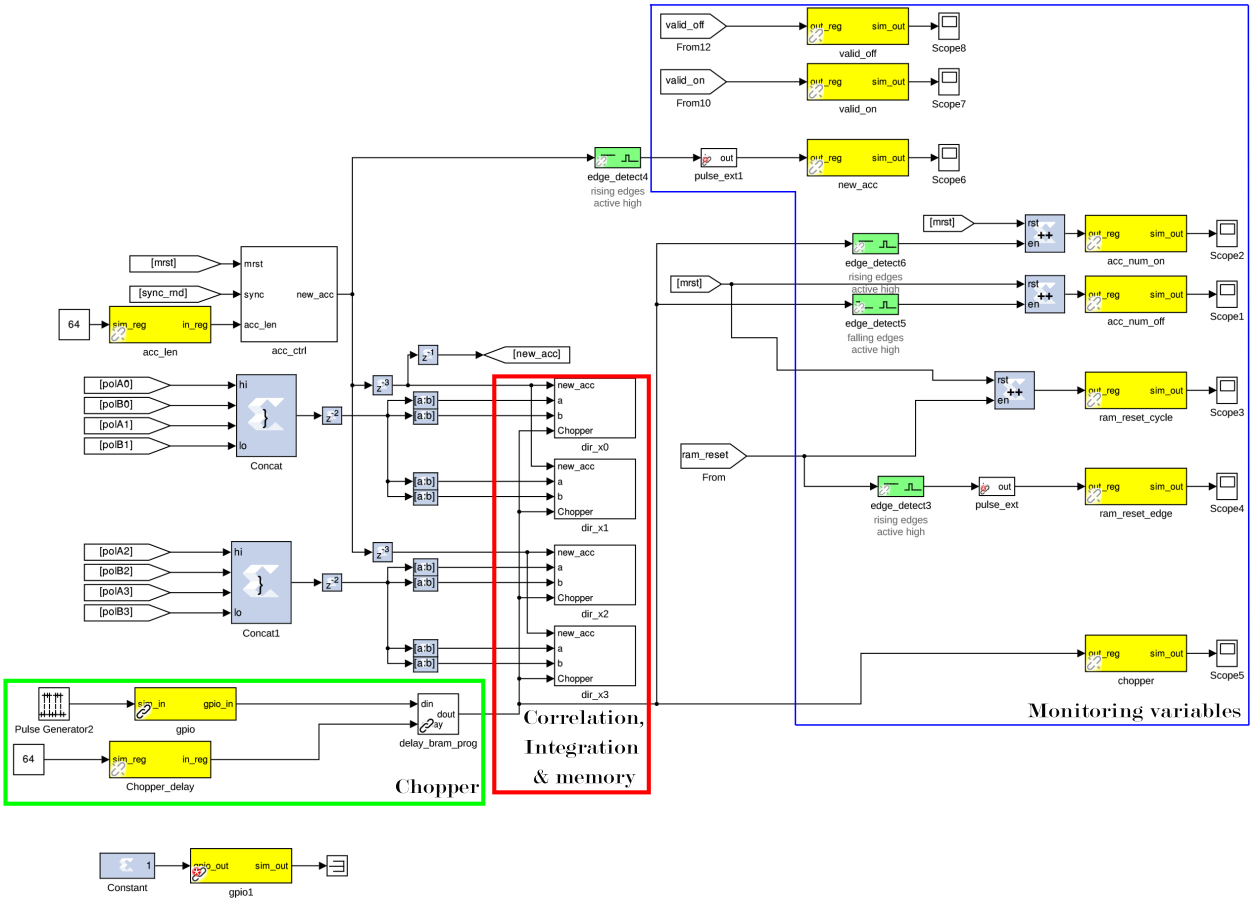

Figure 3.6: Partial correlator's Simulink model.
In green is the chopper digitization section, in red the integration modules and in blue monitoring variables. For a full version see appendix A.

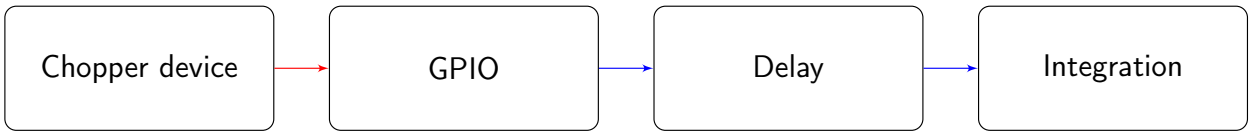

(a) Implementation of the chopper detection in the ROACH.

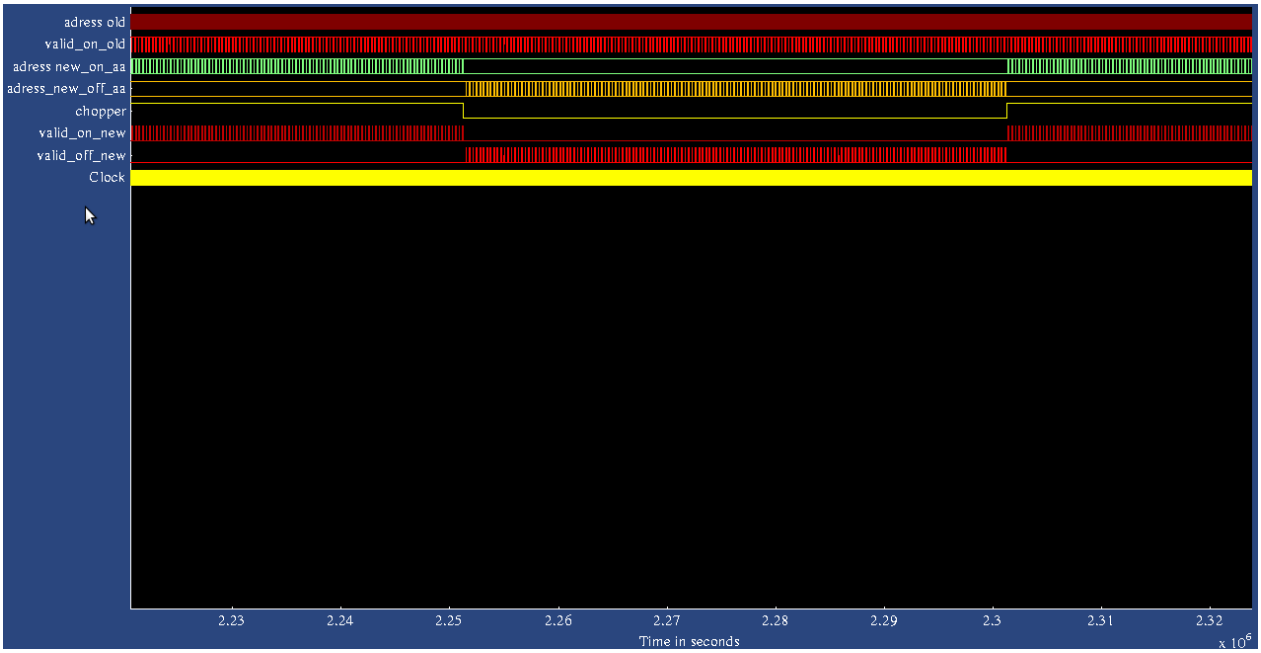

(b) Chopper and integration datapath.

Figure 3.7: Chopper integration on interferometer model.

3.3.2 Integrator and Memory allocation

The original correlation modules from CASPER where intended for continuous measurements (Figure 3.8a). Therefore the accumulation reset is defined by software and the signal (new_acc) is generated within the FPGA. The proposed correlator requires the handling of two different integration states determined by the chopper. Early models used two pocket correlator integration and memory modules (Figure 3.8b), comparing the chopper signal to new_acc determining when to perform a new accumulation. After some tests, it was discovered that this approach couldn't manage the accumulations properly, and to solve this problem the new accumulation signal had to be replaced by an in house design.

This new signal is the output of a simple logical circuit (Figure 3.9). This circuit detects a raising or falling edge from the digitized chopper signal. When an edge is detected, rising for "on" and falling for "off", a guard two times the FFT-channels width processing time is introduced to clean all accumulation registers and prevent inter-state interference. When the opposite edge is detected, falling for "on" and rising for "off", the integration stops and the values are maintained in a random access memory (RAM) register until the next edge is detected.

Including all these new elements into the model enabled a new correlator architecture, with 800 MHz IF-bandwidth, 256 FFT-channels and 36 bit FFT output. This correlator was tested under the experiments described in the next chapter.

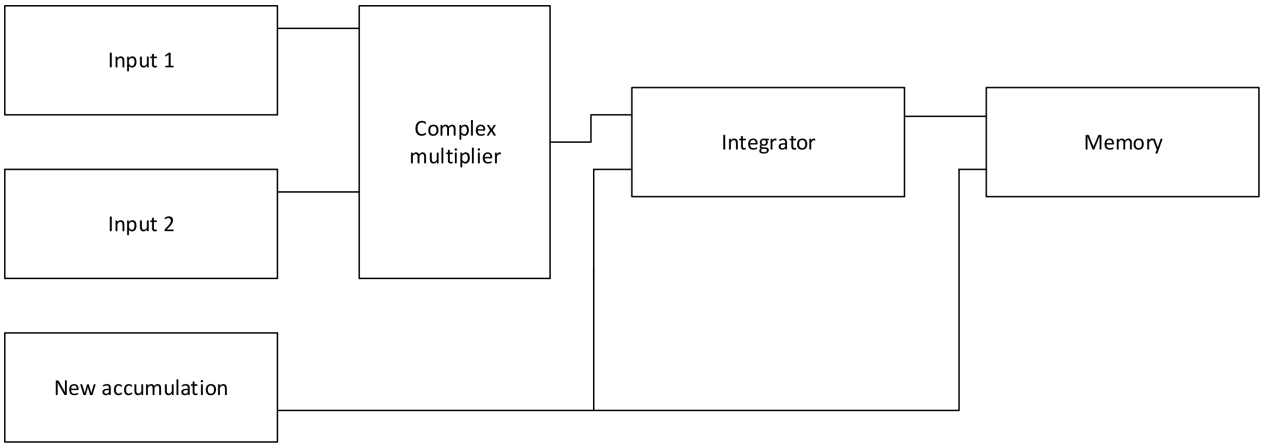

(a) Original integration module from CASPER.

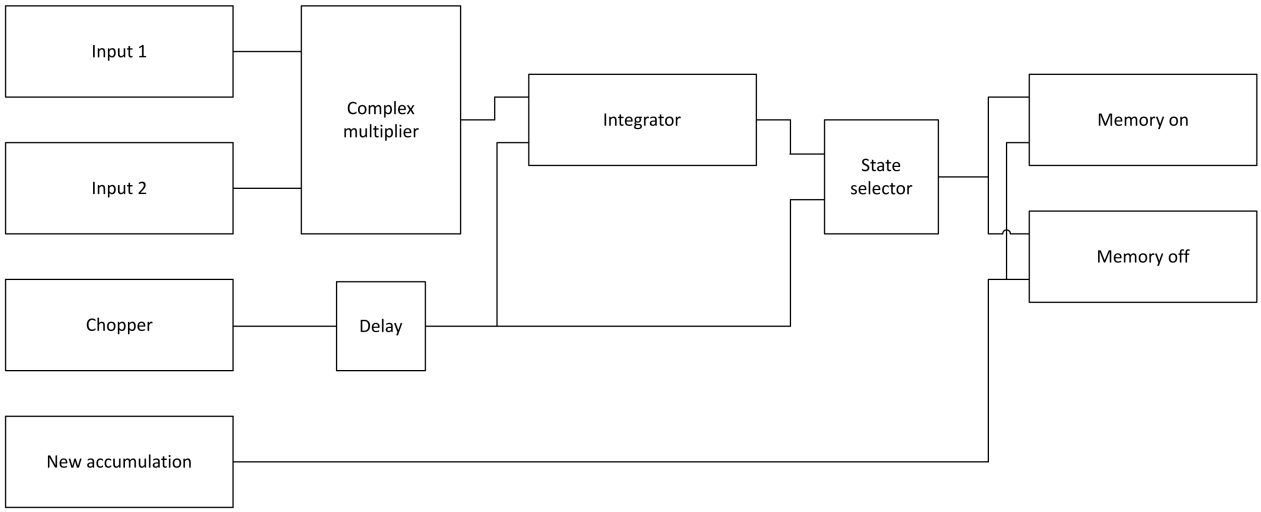

(b) Modified integration module.

Figure 3.8: Auto-correlation integration module comparison.

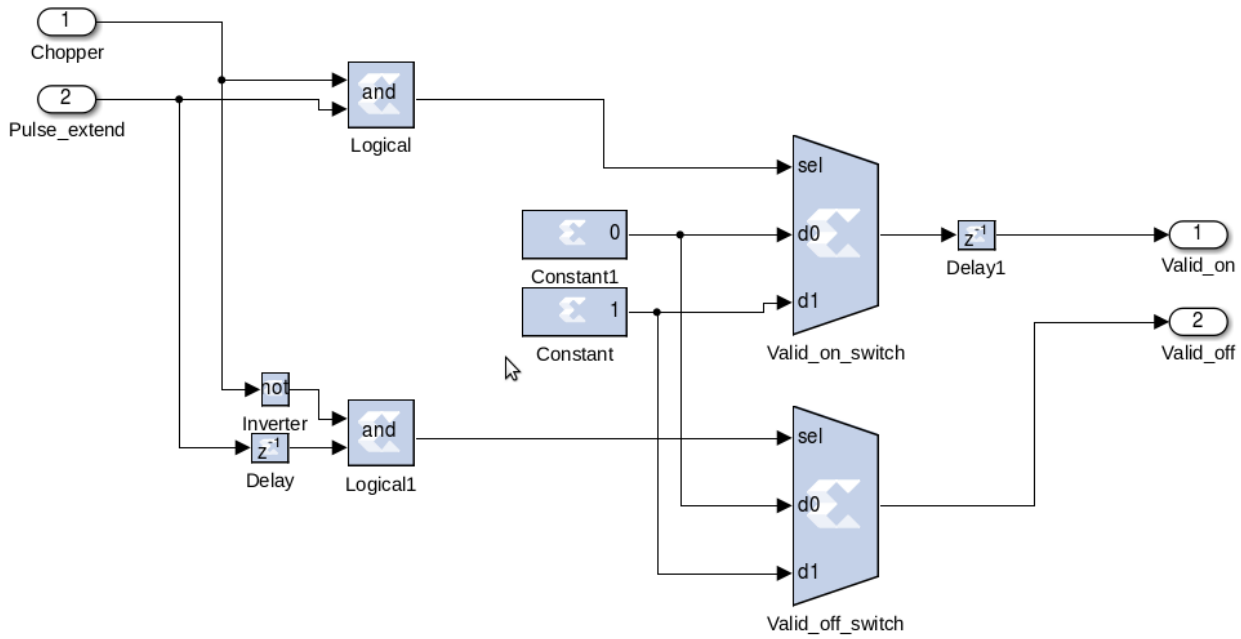

Figure 3.9: Logical circuit for the on-off selector in the integration module.

Chapter 4

Lab characterization of the detection system

The first step to validate the correlator in a laboratory environment is the calibration of the ADCs (section 4.1). After the system was calibrated, different experiments were held to get the system's performance (section 4.2, 4.3 & 4.4)

4.1 Calibration of the ADC 0 dBm level

The correlator is a digital circuit, therefore the output are only numbers without meaning. To give these values a significance, the system had to be calibrated. The selected source for this case was a 5008 Valon dual Frequency synthesizer Module (Figure 4.1). The synthesizer was set to 600 MHz and an output level of nominally 0 dBm. The synthesizer's output power was measured with an ESA. Afterwards the same signal power was measured with one of the ROACH's auto-correlation channels. As the synthesizer's signal was slightly off the 0 dBm level, both measurements were substraced to obtain the real 0 dBm level. The integration (chopping) frequencies were selected from the technical requirements of the experiments (0.5, 1, 3.3 and 8 Hz). The reference output power of the signal synthesizer was -1.04 dB for every frequency except 8 Hz, were the power was -2 dBm. As a result the table 4.1 was obtained. The value for 8 Hz is higher, because the signal was less attenuated at the ADC input. For the first 3 chopping frequencies a 10 dB attenuator was used, but for the last frequency a 5 dB attenuator was used. These attenuators were used to prevent any damage on the ADCs. To prevent aliasing the inputs have also a low-pass filter with an 800 MHz cut-off frequency.

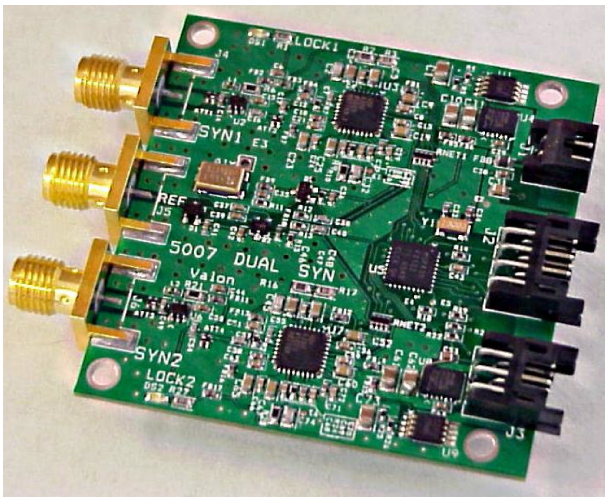

Figure 4.1: Valon dual Frequency synthesizer module [40].

Frequency [Hz]	ADC attenuator [dB]	ROACH measured power [dB Arbitrary units]	0 dBm level in dB [dB Arbitrary units]
0.5	10	125.585	126.625
1	10	122.6	123.64
3.3	10	120.179	121.219
8	5	121.206	123.206

Table 4.1: 0 dBm level for different chopping frequencies.

4.2 FFT integration measurements

With the system calibrated, it was necessary to test its real capabilities to detect a star signal. Prior to any on-sky measurement a laboratory test had to be held, aiming at characterizing the system against known sources. To simplify these experiments, the air-to-fiber coupling sub-systems were not connected to the receivers. Instead, the noise source was split through a 50/50 fiber-splitter and directly connected to each receiver.

After carefully considering the different alternatives available in the lab, two sources were selected. The first was an EXALOS Superluminescent light emitting diode (SLED) (model EXS1550-060-20-0201130) (Figure 4.2a). This SLED has its central wavelength at 1550 nm and 60 nm Full With Half Maximum (FWHM) bandwidth. As the correlator has only 1.6 GHz Double side band (DSB) bandwidth, this source can be regarded as a continuum-noise source. One feature of the SLED is a TTL shutter, enabling to start and stop the light emission with a digital input, thus emulating a chopped star. For this source, a digital 1 Hz chopping signal was selected, due to a small transient when switching on and off the SLED. A second set of results was taken with an Ocean Optics HL-2000 halogen lamp, which was coupled to a mono-mode fiber. This source was measured with an 8 Hz chopping frequency, using an external mechanical chopper wheel from Stanford Research Systems (model SR540), depicted in Figure 4.2b. This

chopping frequency was selected, as it is the maximum communication speed between the ROACH and the controlling computer.
The optical power was measured using a Thorlabs Powermeter (model PM100D with a S154C fiber photodiode sensor). When the signal was smaller than 1 nW, an Anritsu Optical Spectrum Analyser (OSA) (model MS9740A) was used to measure the optical power.

At the receiver the signal was mixed with the master laser reference, a NKT Photonics Koheras Adjustik (Figure 4.2c), by using a tunable fiber beam-splitter and coupled into a balanced photodiode. To maximize the photodiodes efficiency, each input receives approximately 950 µW of LO power. The IF signal is then amplified by 62 dB, digitized and processed by the ROACH-based correlator. The system runs for 10 to 30 minutes and afterwards the data is post-processed to get the results.
Interesting features are; differences between on and off measurements, power levels and differences between receivers.

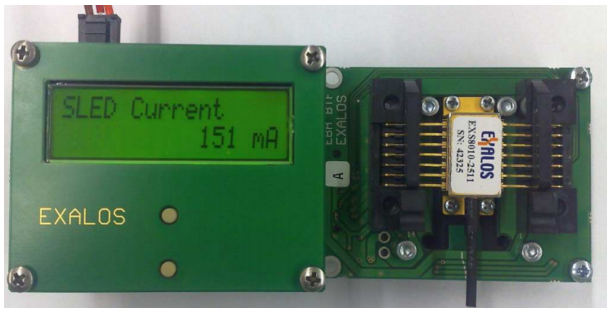

(a) EXALOS SLED with driver.

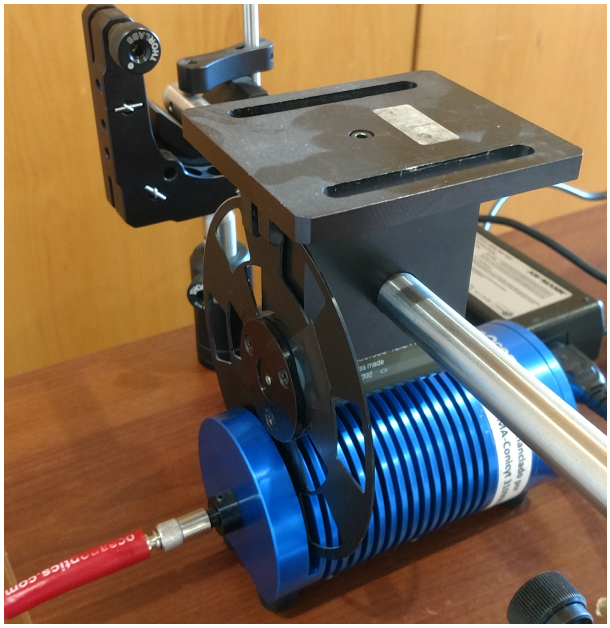

(b) Ocean Optics HL-2000 halogen source with chopper wheel.

(c) Koheras Adjustik Laser.

Figure 4.2: Light sources.

The results for this experiment are depicted in a set of four plots. Figures "a" and "c" show the calibrated auto-correlation and cross-correlator measurements (on - off). Figures "b" and "d" show the mean power spectrum for both measurement states, "on" and "off".

The best results for the SLED are shown in Figure 4.3, for a measured power of 400 nW (200 nW per receiver). In figures 4.3a & 4.3c are clearly noticeable the amplifier's pass-band and spurious peaks. As these plots show the final measurement, it is not possible to determine the origin of these unwanted signals. To observe the spectra in detail and understand the noise origin, the "on" & "off" measurements have to be separately plotted (Figures 4.3b & 4.3d). In auto and cross-correlation it is possible to distinguish clearly between two different states, where "on" has a higher spectral power than "off".
For auto-correlation, channel B has a slightly stronger difference between both states (0.1 dB against 0.05 dB). The Y-axis between both channels shows also a 0.5 dB difference, due to mismatches between the amplification chains. Channel A has peaks at 175, 525 and 800 MHz which are not present in channel B. These peaks show a shielding problem on this channel, from leakage of a radio frequency (RF) signal through the coaxial cable and the subsequent amplification. The 400 MHz peak at both channels is a digital spurious signal generated by the ROACH.
The cross-correlation (Figure 4.3d) has a 14 dB lower noise level. However it has more features, probably due to the influence of (standing waves) phase effects, which as a result yields a Φ=0 for all FFT-channels. These perturbations show up as a 3 dB high profile in the IF. The instabilities below 30 MHz are some kind of computational error, as the amplifiers have an operating range between 30 MHz to 3 GHz. The 3 dB positive slope between 30 to 400 MHz has an unknown origin and further tests have to be performed to find out its source. The roll-off from 500 MHz to 800 MHz is normal, as the ADC-input has an 800 MHz low-pass RF-filter to prevent aliasing.

In the case of the Halogen lamp, the signal power was measured to 854 fW (427 fW per receiver), using an OSA (Anritsu MS9740A) over a 0.02 nm spectral-channel. For this source "on" and "off" are still distinguishable from one another, with a 0.1 dB difference in auto and cross correlation (Figures 4.4b & 4.4d). This source has a better performance, due to the mechanical chopper, as there is no transient between states. Therefore there is less cross talk between "on" and "off" states. The external perturbations are similar to the SLED measurement, with peaks at 50, 250, 400 and near 800 MHz. For this case the peaks in channel A are more powerful than the ones in channel B. In the auto-correlation there seems to be some kind of heavy perturbation in channel A (220 to 300 MHz) which is not present in channel B. For cross-correlation, the system detects correctly the low edge of the band-pass filter, but for the other end, a 5 dB roll-off is detected instead of the normal 3dB, which for now is not possible to understand.

Comparing both sourced, with similar sensitivity level (difference between on and off to 0.1 dB), it is possible to find 2 key differences:

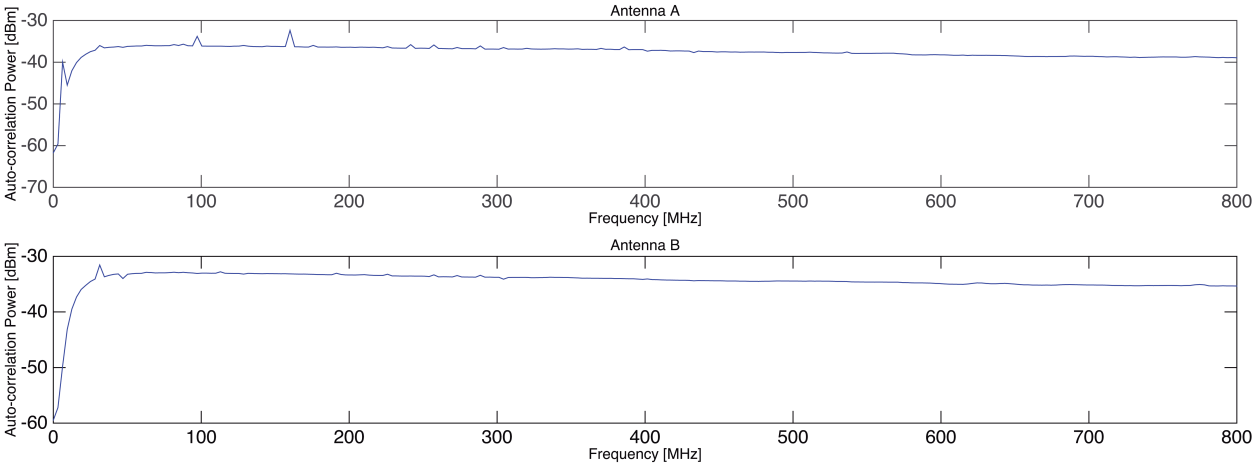

(a) Auto-correlation measurement.

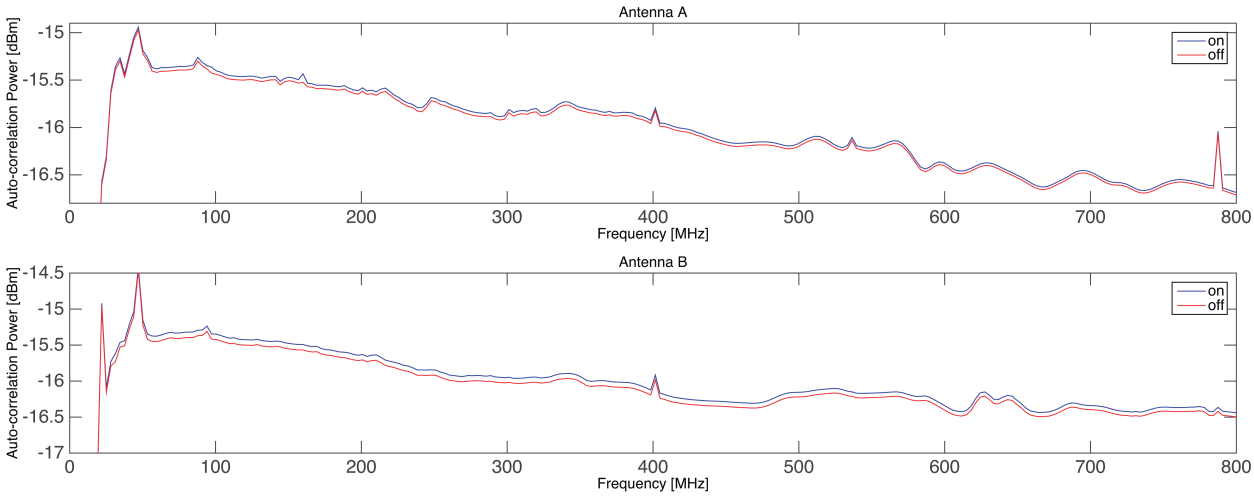

(b) Auto-correlation on and off measurement.

Figure 4.3: Integration results for SLED source at 400 nW total power.

- Source input power: The source power for both cases is quite different for similar FFT sensitivities. For the SLED, the input power is measured to 400 nW and the Halogen source is 854 fW. These input differences are probably caused by the transient of the SLED between states.
- Phase: For the SLED the phase is always the same (Φ=0), while the Halogen lamp shows phase-changes for power fluctuations. This difference is probably caused by the influence of standing waves on the SLED.

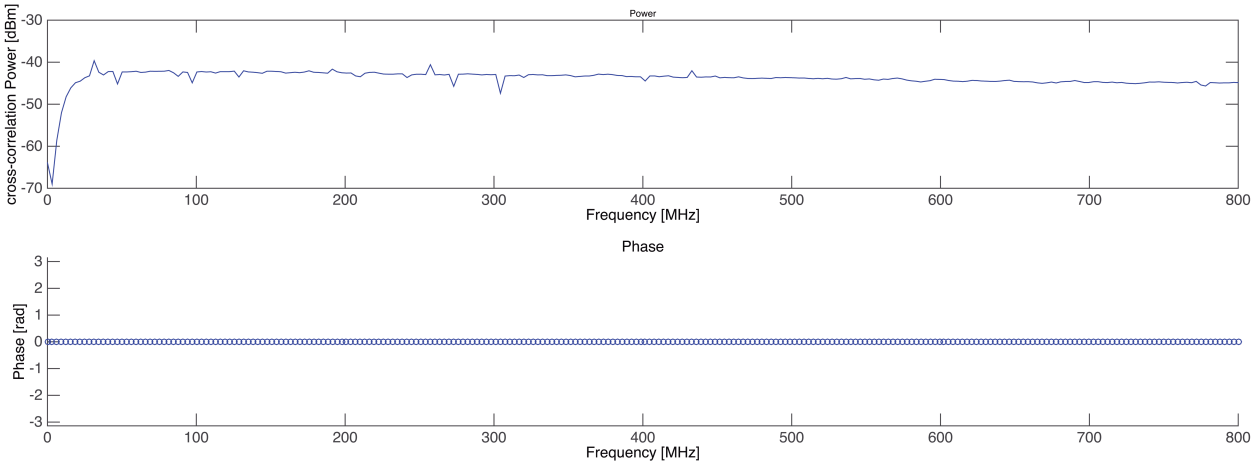

(c) Cross-correlation measurement.

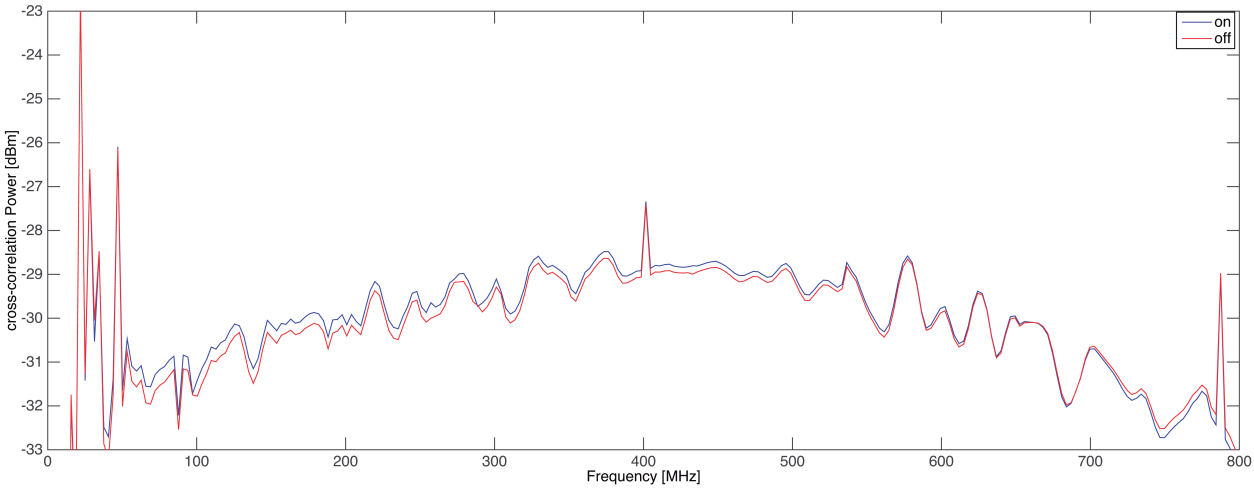

(d) Cross-correlation on and off measurement.

Figure 4.3: Integration results for SLED source at 400 nW total power.

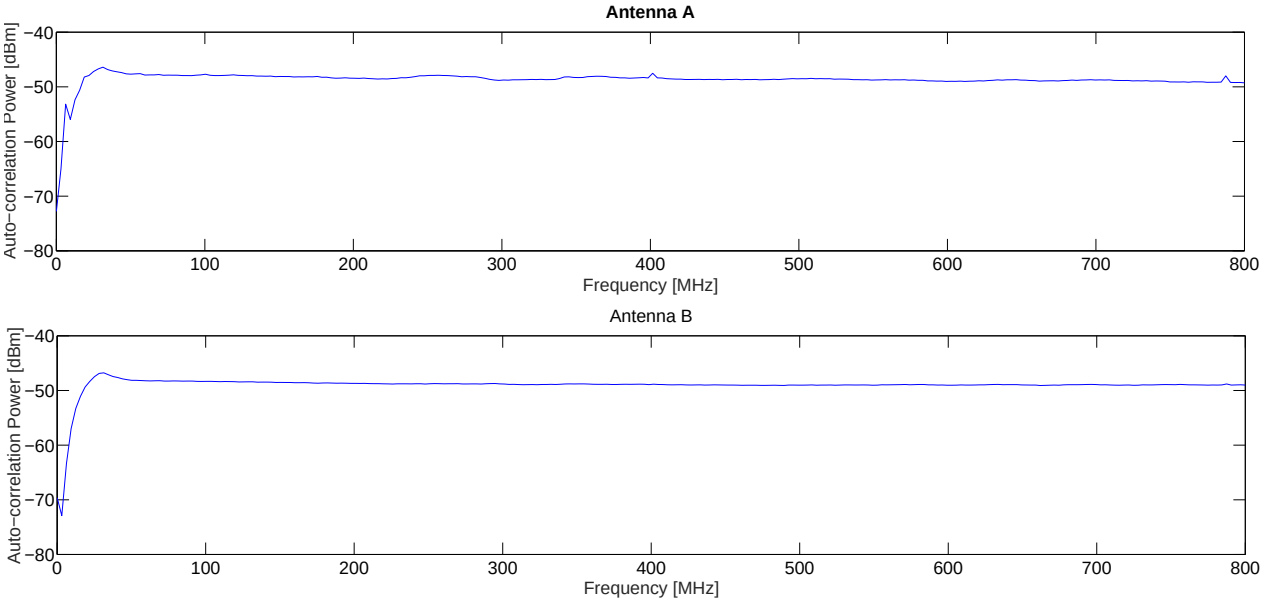

(a) Auto-correlation measurement.

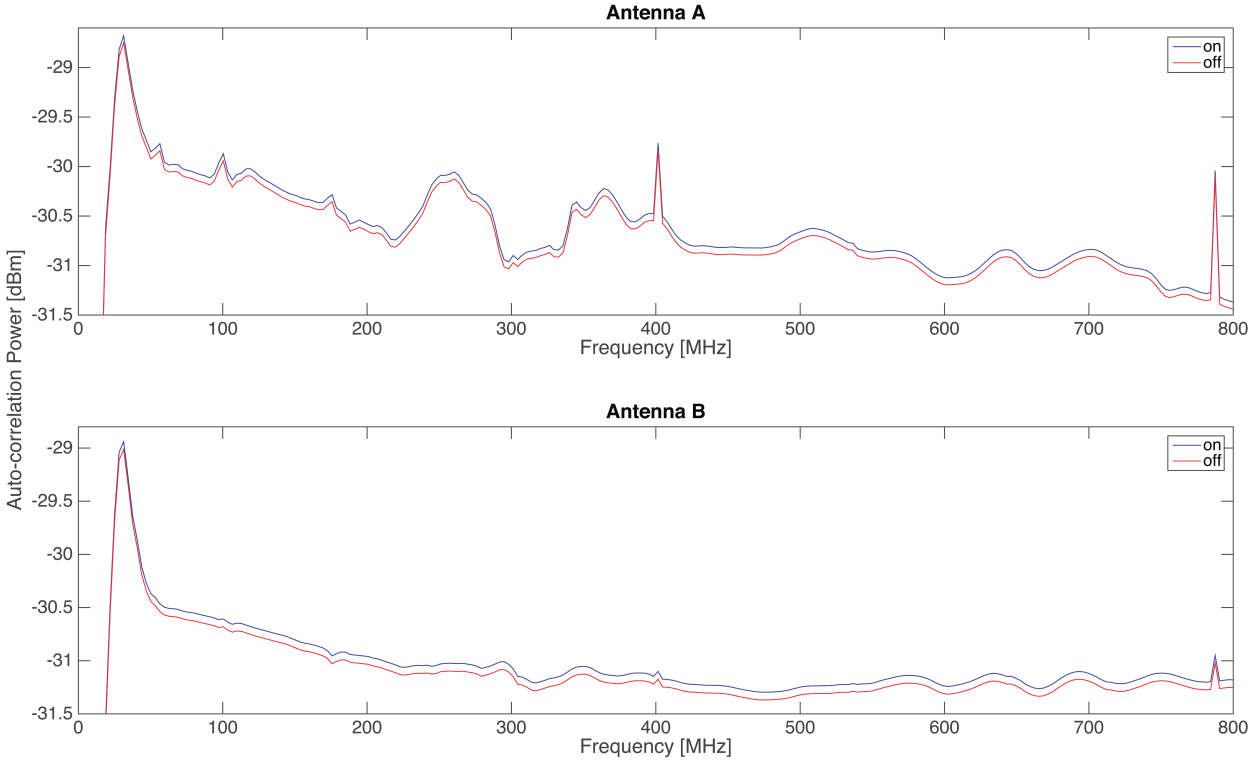

(b) Auto-correlation on and off measurement.

Figure 4.4: Integration results for Halogen source at 854 fW, for a 0.2 nm spectral channel.

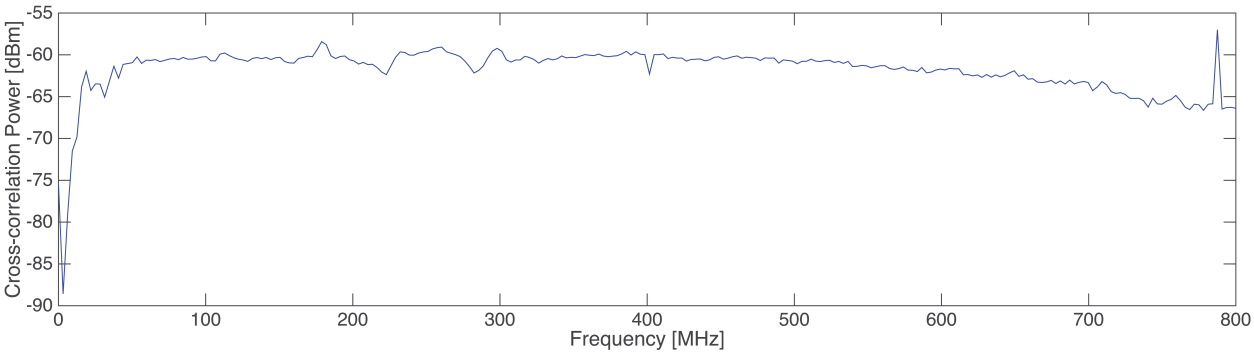

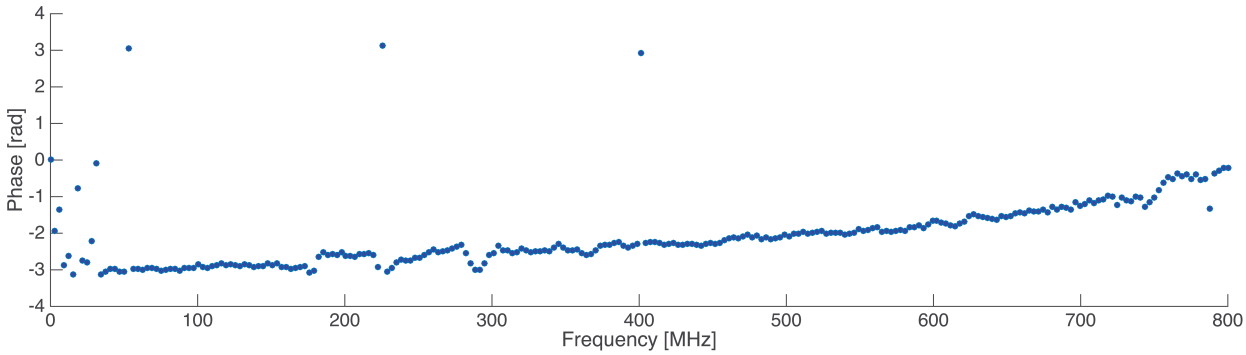

(c) Cross-correlation measurement.

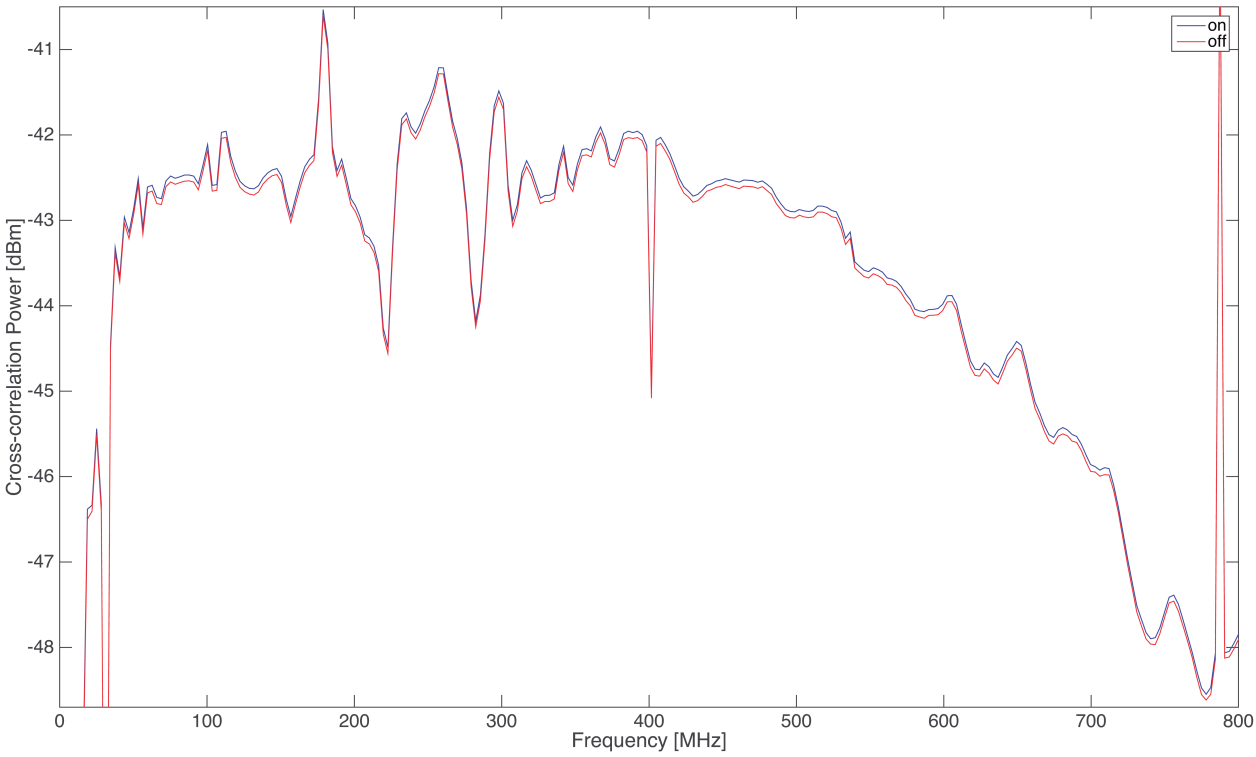

(d) Cross-correlation on and off measurement.

Figure 4.4: Integration results for Halogen source at 854 fW, for a 0.2 nm spectral channel.

4.3 Allan variance Plots

In order to get enough data to make the Allan variance plots, the correlator experiment has to run through the night. For this case, the selected source was the Ocean Optics HL-2000 halogen lamp (Figure 4.2b), using the same experimental set-up from the previous section. Using the algorithm explained in section 2.5 for the sum of all channels, the data is processed and the resulting values are then plotted against the integration time.

The Allan variances were expressed in 3 graphs, one for each auto-correlation (Figure 4.5a & 4.5b) and the third for cross-correlation (Figure 4.5c). For the auto-correlation it is possible to see the classical Allan variance tendency, as shown in Figure 2.7, with an Allan time of approximately of 1500 - 2000 seconds. This tendency is not clearly noticeable in the cross-correlation, as it plateaus at a similar integration time as the auto-correlation, but then steps down instead of climbing.
Under the assumption that this second fall is still relevant, despite the relatively small amount of calculated samples, it is possible to describe an Allan time bigger than 2000 seconds for the cross-correlation total power measurements. To determine the real cross-correlation Allan time, longer runs are needed (e.g. 24 hours), but at the time these runs were not possible.

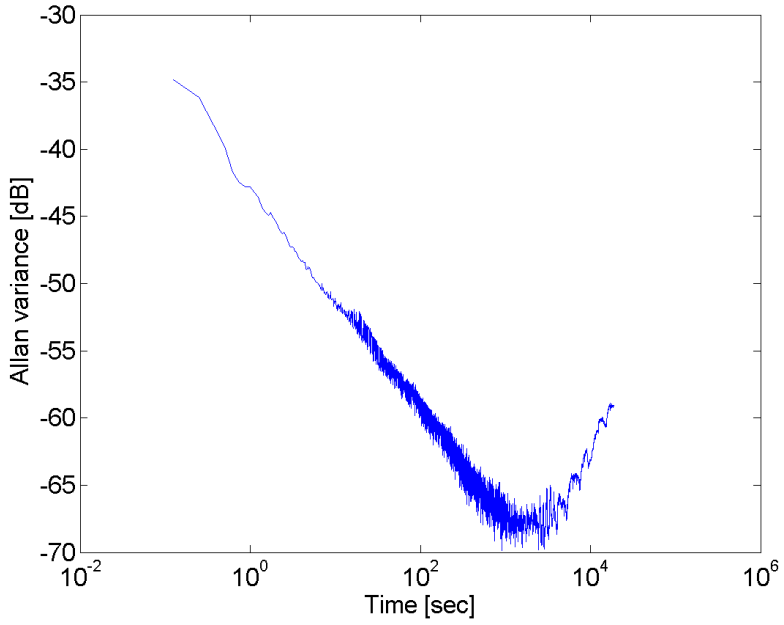

(a) Auto-correlation antenna A.

Figure 4.5: Total power Allan plots of the system.

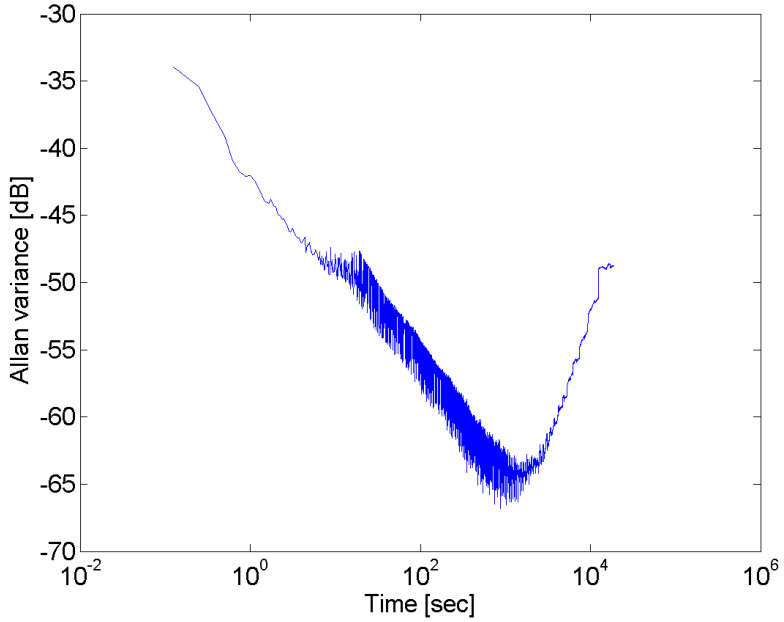

(b) Auto-correlation antenna B.

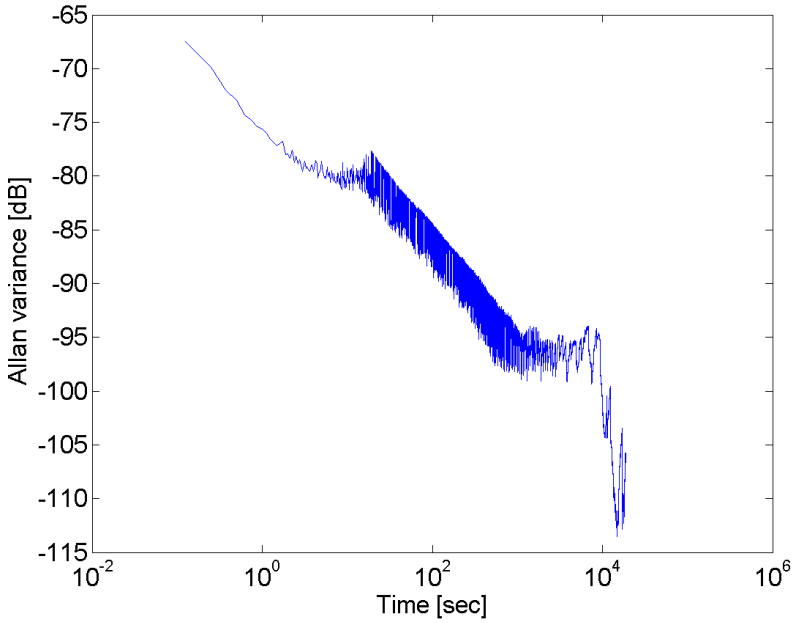

(c) Cross-correlation.

Figure 4.5: Total power Allan plots of the system.

4.4 Receiver noise temperature

To reach the final goal of correlating a star, the sensitivity of the detection and correlation system had to be measured. To achieve this, several measurements were done for optical input power values between 20 fW to 1 pW, therefore each recevier's input power was between 10 to 500 fw. For each power value the system ran for 1000 seconds and the data was processed with the algorithm explained in 4.2, but selecting only the top 1 dB values.
The results were represented by plotting the mean output power over the optical input power. This plot should show a positive constant slope. The expected mean power for auto-correlation are higher than for cross-correlation, due to a higher noise influence in auto-correlation.
In auto-correlation, the main noise contribution comes from the laser's shot noise, described as partition noise from the beam-splitter. The excess noise of the laser is common mode and subtracted (25dB) by the balanced photodiodes.

As explained in subsection 2.4.1, a hot-cold measurement was used to determine the receiver temperatures, where P_{hot} and P_{cold} are the post-processed power output for a 50 MHz Brimrose Fiber Frequency Shifter (FFS) (model AMF-55-SM-2FP) source and an adjacent correlator's zero power input channel respectively. A FFS is an acousto-optical modulator device, which uses Doppler Shift to diffract the beam and shift it in frequency by the acoustic carrier frequency [41]. The FFS is fed with a small laser signal split from the Koheras laser and damped down with optical-attenuators. In this case the chopping was not possible, but this didn't represent a problem as the signal had a single spectral channel width on the correlator. Nevertheless, to use the designed correlator model an 8 Hz chopping frequency was selected.
According to theory, the zero input power divided by the slope is proportional to the system noise temperature, and to compare it against the theory the noise temperature quantum limit for a λ=1.55 µm receiver was calculated using (2.16), yielding a double-sideband equivalent receivers temperature (T_Q) of 4612 K.

To calibrate T_{rec}, the source power was measured as precisely as possible, while $\Delta\nu_s$ was assumed to be twice the correlator channel-width, due to DSB-detection (2·3.125 MHz = 6.25 MHz). The frequency shifted laser was assumed to be very stable and sharp within one spectral channel of the ROACH.

Figure 4.6 shows the post-processed mean power of the ROACH FFS channel, and Figure 4.7 the signal spectra for an FFS optical power of 28 fW. As expected, the cross-correlation output noise power was an order of magnitude lower than the auto-correlation, since cross-correlation integrated measurements eliminate un-correlated fluctuation between both receivers, adding less noise to the processed power. The plateau centred at 176 fW could be a coupling problem with the optical attenuators used for this experiment, as plug-in optical attenuators were used instead of a tunable one. Despite this problem, it is possible to define the +3 dB point for each correlator's matrix element.
In auto-correlation, the +3 dB level, would be around 0.015 mW which corresponds to a signal power

of approximate 500 fW for channel A and 250 fW for channel B. In the cross-correlation, the +3 dB level would be 0.0016 mW, which corresponds to so source power of approximately 14 fW. The receiver's temperature for these source powers are given in table 4.2. The difference between A and B could be related to an unbalanced detector, or a lower LO signal power delivered to one of them.

Element	$\mathbf{P_{ffs}/2}$	$\mathbf{T_{rec}}$	T_{rec}/T_Q
Auto-correlation antenna A	500 pw	12072 K	2.62
Auto-correlation antenna B	250 fw	6036 K	1.31
Cross-correlation	14 fw	338 K	0.07

Table 4.2: Auto and cross-correlation receivers temperature.

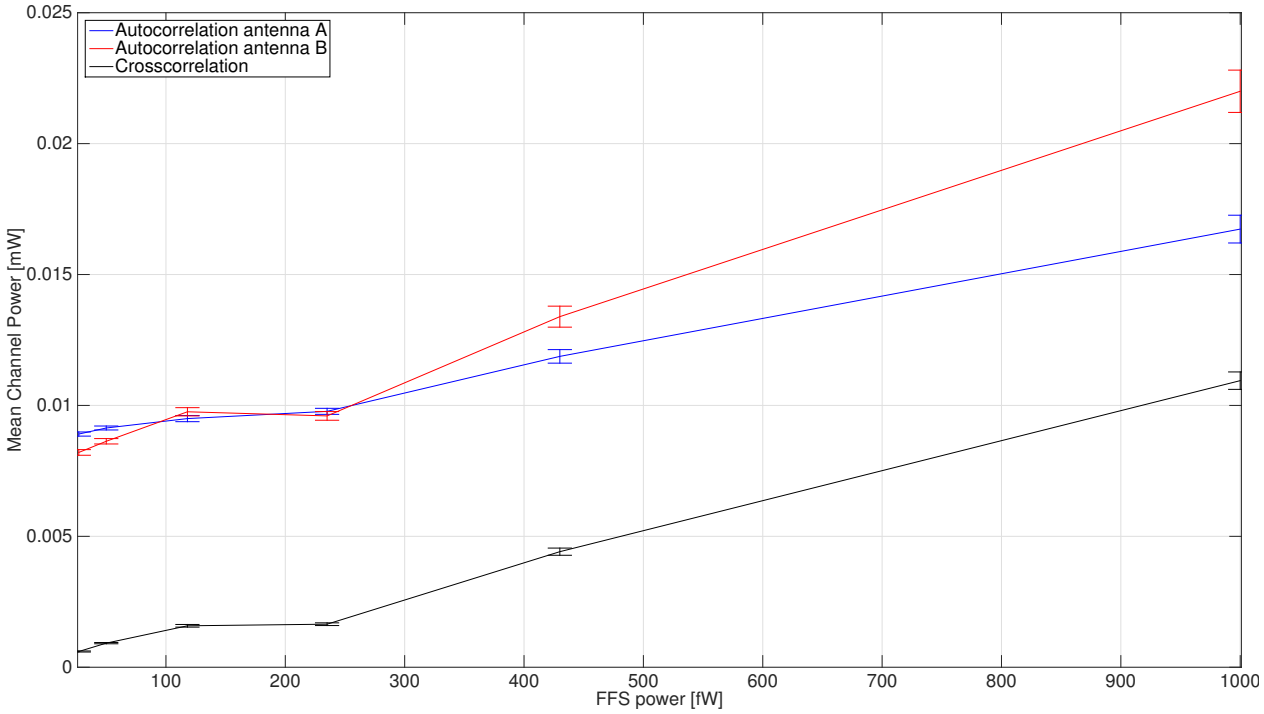

Figure 4.6: Channel Power for a single channel of the ROACH, using a FFS as a source.

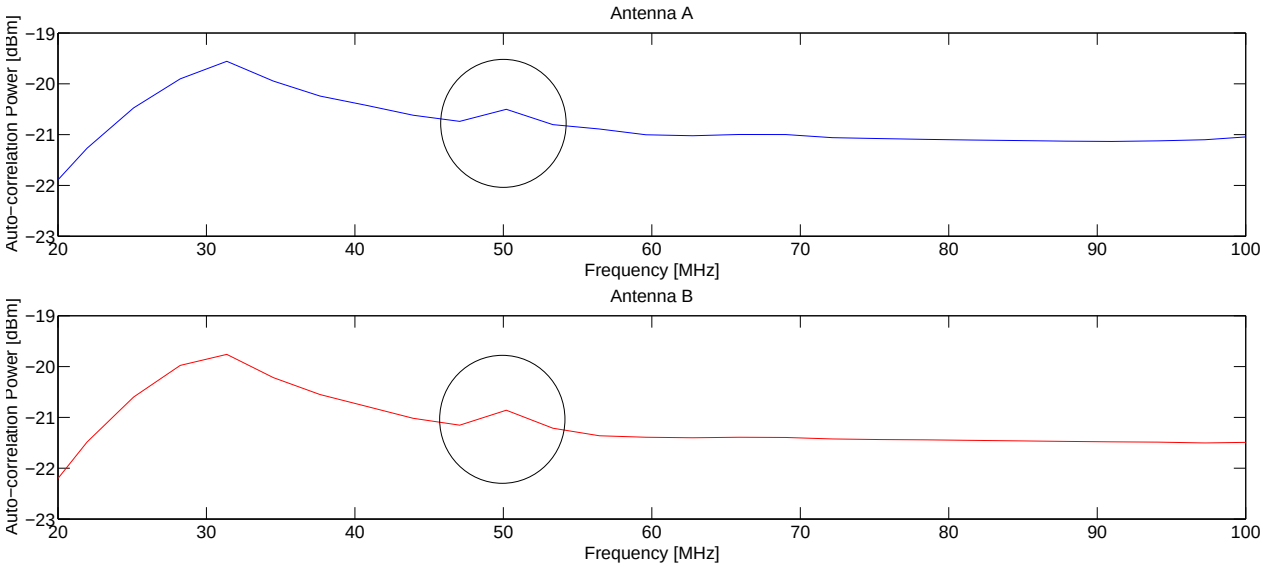

(a) Auto-correlation measurement.

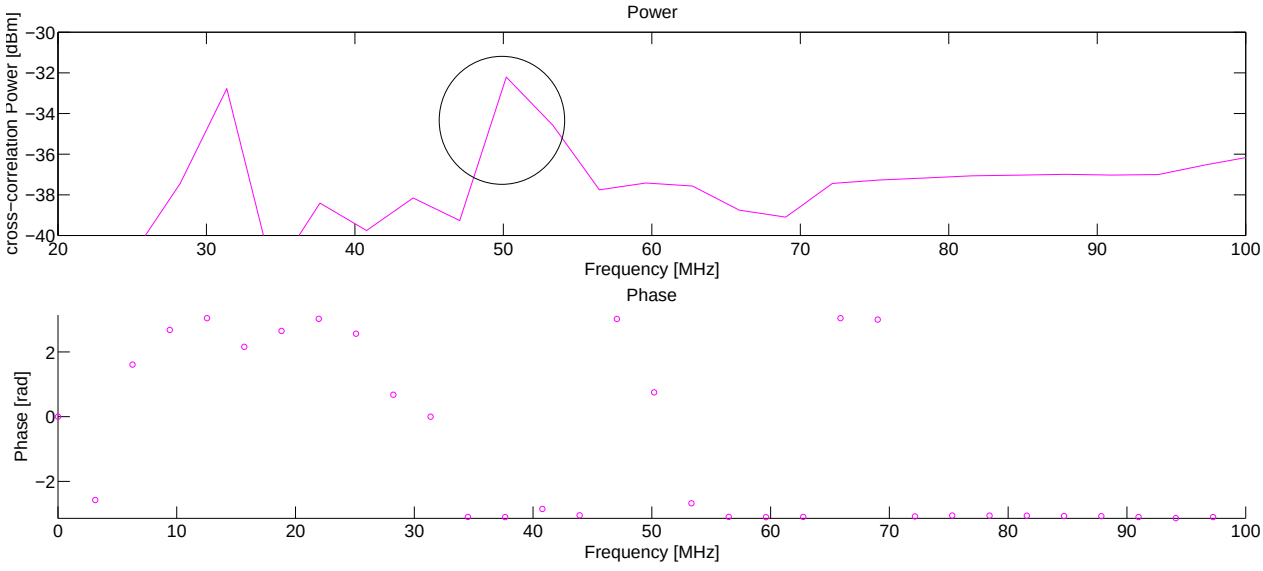

(b) Cross-correlation measurement.

Figure 4.7: Integration results for a FFS source at 27 fW optical power. Encircled is the detected 55 MHz signal

Chapter 5

Conclusions

Infrared heterodyne interferometery has been demonstrated for the first time some 30 years ago, but our interferometer is the first one being built in Chile.
We designed and implemented in our laboratory a novel double-balanced photodiode two-receiver detection system together with a digital correlator based in a ROACH1-board, and tested and improved it extensively for similar light-starved conditions as in a starry night. The results obtained show a system capable of detecting signals at a fW per channel level, with near to shot-noise sensitivity at auto-correlation and sub-shot-noise (sub quantum limit system noise temperature) sensitivity at cross-correlation. As especially the last finding is astonishing and hard to believe, as it seems to contradict quantum mechanics, we did a lot of verifying work in this respect, which comprised using three different types of radiation test sources and their meticulous calibration.

The Allan times of the system in our lab were more than satisfactory, with more than 1000 seconds in autocorrelation, and 2000 seconds in cross-correlation. This was possible after adding to the correlator model an ON/OFF-switch scheme (known as a Dicke-switch from radio astronomy). Of course these values could be better, but the essence of these results shows that a digital based correlator, in conjunction with our novel receiver configuration, should operate very well in correlating a star light signal.

Follow-up work is of course necessary towards this goal. First, it is important to drive the performance of the correlator even closer to its limits, by improving the communication between the computer and the ROACH and by further optimizing the digital model, e.g. to eliminate some spurious common-mode digital noise supposedly having to do with fluctuating integration periods of the On/Off-switch (in our test setup the optical chopper or the trigger of the SLED, but later an on-sky position switch). Finally, it is important to combine and test the detection system containing this correlator with our two 35 cm-aperture telescopes and demonstrate the complete system on-sky, showing that the whole heterodyne interferometer is able to detect Betelgeuse with reasonably short integration times.

Outlook: As we have a road-map towards a 3 telescope system, an extension to a 3 or 4 telescope correlator will be performed using a ROACH2 board (developed for SKA), in the configuration with two 5 Gsps ADCs split each into two sub-ADCs working at 1250 MHz bandwidth. With that working hopefully without problems, the motivation would be then to include also a closure phase feature into the correlator model.

Appendix A

Correlator's Simulink model

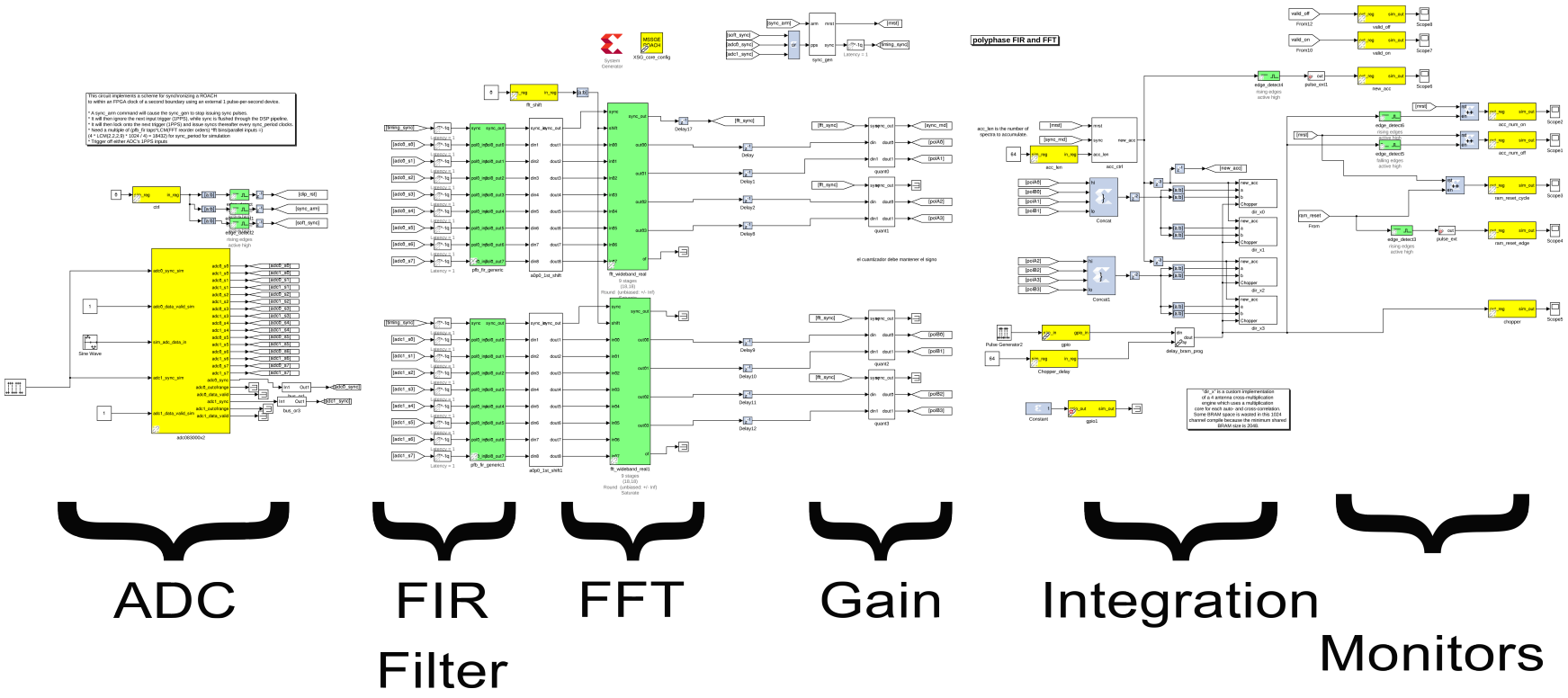

Figure A.1: Correlator's Simulink full model

Acronyms

ACA Atacama compact array.
ADC Analog to Digital Converter.
ALMA Atacama Large Millimeter and submillimeter Array.
AO Adaptive Optics.

CASPER Collaboration for Astronomy Signal Processing and Electronics Research.
CCD Charged Coupled Device.
CHARA Center for High Angular Resolution Astronomy.

dc direct current.
DSB Double side band.

E-ELT European-Extremely Large Telescope.
ESA Electrical Spectrum Analyser.

FFS Fiber Frequency Shifter.
FFT Fast Furier transform.
FM Frequency modulation.
FMI Fiber-based Michelson's interferometer.
FN Flicker noise.
FPGA Field Programmable Gate Array.
FWHM Full With Half Maximum.
FzI Fizeau's interferometer.

GPIO General Purpose Input/Output.
Gsps Giga samples per second.

HARPS High Accuracy Radial velocity Planet Searcher.
HI Heterodyne interferometer.

IF intermediate frequency.
IR infrared.
ISI Infrared Spatial Interferometer.

LLC line-length correction.
LO local oscilator.

mas milli-arc-second.
MI Michelson's interferometer.

nep noise equivalent power.
NIR near infrared.

OPD Optical path difference.
OPL Optical path length.
OSA Optical Spectrum Analyser.

PD photodiode.
PFI Planet Formation Imager.
PID Proportional Integrator and Derivative.
PM Phase modulation.

RAM random access memory.
RF radio frequency.
RFI Radio Frequency Interference.
ROACH Reconfigurable Open Architecture Computing Hardware.
RWN Random walk noise.

SKA Square Kilometer Array.
SLED Superluminescent light emitting diode.

SM sinlge-mode.
SMA Sub-miniature A.
SNR Signal to Noise ratio.

TTL Transitor transistor logic.

VLA Very large array.
VLBI Very long baseline interferometer.
VLTI Very Large Telescope Interferometer.

WN White noise.

Bibliography

[1] J. D. Monnier, S. Kraus, D. Buscher, J.-P. Berger, C. Haniff, M. Ireland, L. Labadie, S. Lacour, H. L. Coroller, R. G. Petrov, J. oerg Uwe Pott, S. Ridgway, J. Surdej, T. T. Brummelaar, P. Tuthill, and G. van Belle, "Planet Formation Imager (PFI): Introduction and Technical Considerations," p. 10, jul 2014.

[2] J. D. Monnier, M. J. Ireland, S. Kraus, F. Baron, M. Creech-Eakman, R. Dong, A. Isella, A. Merand, E. Michael, S. Minardi, D. Mozurkewich, R. Petrov, S. Rinehart, T. ten Brummelaar, G. Vasisht, E. Wishnow, J. Young, and Z. Zhu, "Architecture design study and technology road map for the Planet Formation Imager (PFI)," p. 99071O, 2016.

[3] E. A. Michael, F. Besser, R. Prado, and L. Pallanca, "Concept for fiber-based near-infrared interferometry of highest frequency resolution," *SPIE Astronomical Telescopes + Instrumentation*, vol. 9146, p. 914634, 2014.

[4] F. E. Besser, A. Rates, N. Ortega, M. I. Pina, C. Pollarolo, M. Romero, C. Yañez, M. Lasen, N. Ramos, and E. A. Michael, "Fiber-based heterodyne infrared interferometry: an instrumentation study platform on the way to the proposed Infrared Planet Formation Imager," vol. 9907, p. 99072L, 2016.

[5] M. Mayor and D. Queloz, "A jupiter-mass companion to a solar-type star," *Nature*, vol. 378, no. 6555, pp. 355–359, 1995.

[6] R. P. Butler and G. W. Marcy, "A Planet Orbiting 47 Ursae Majoris," *The Astrophysical Journal*, vol. 464, no. 2, pp. L153–L156, 1996.

[7] J. I. Hernández, G. Israelian, N. C. Santos, S. Sousa, E. Delgado-Mena, V. Neves, and S. Udry, "Searching for the signatures of terrestrial planets in solar analogs," *Astrophysical Journal*, vol. 720, no. 2, pp. 1592–1602, 2010.

[8] L. Ricci, L. Testi, A. Natta, A. Scholz, and I. de Gregorio-Monsalvo, "ALMA observations of ρ-Oph 102: grain growth and molecular gas in the disk around a yound brown dwarf," *The Astrophysical Journal*, vol. 761, no. 2, p. L20, 2012.

[9] R. A. Serway and J. W. Jewett, *Physics for Scientist and Enginners*. David Harris, 7 ed., 2008.

[10] J. D. Monnier, *Infrared interferometry and spectroscopy of circumstellar envelopes*. PhD thesis, UNIVERSITY of CALIFORNIA at BERKELEY, 1999.

[11] D. F. Buscher and M. Longair, *Practical Optical Interferometry*. Cambridge: Cambridge University Press, 2015.

[12] J. D. Monnier, "Optical Interferometry in Astronomy," vol. 789, p. 86, 2003.

[13] ISI, "Interferometer Comparison." `http://isi.ssl.berkeley.edu/images/michisifig.gif`.

[14] A. A. Michelson and F. G. Pease, "Measurement of the diameter of alpha Orionis with the interferometer.," *The Astrophysical Journal*, vol. 53, no. 9, p. 249, 1921.

[15] ISI, "4812-lores.jpg (600×403)." `http://isi.ssl.berkeley.edu/images/4812-lores.jpg`.

[16] J. Roberts, "Amateur Astronomer's Notebook." `http://www.rocketroberts.com/astro/ccd_fundamentals.htm`, 2009.

[17] P. Léna, D. Rouan, F. Lebrun, F. Mignard, and D. Pelat, *L'observation en astrophysique*. Savoirs Actuels, EDP Sciences, 2008.

[18] A. Labeyrie, S. G. Lipson, and P. Nisenson, *An introduction to optical stellar inteferometry*. 2006.

[19] C. Townes, M. Bester, W. Danchi, D. Hale, J. D. Monnier, E. Lipman, P. Tuthill, M. Johnson, and D. Walters, "Infrared Spatial Interferometer," in *Proc. SPIE Vol. 3350, p. 908-932, Astronomical Interferometry, Robert D. Reasenberg; Ed.*, vol. 3350, pp. 908–932, 1998.

[20] a. R. Thompson, J. M. Moran, and G. W. Swenson, *Interferometry and Synthesis in Radio Astronomy*. 2001.

[21] R. P. Escoffier, G. Comoretto, J. C. Webber, A. Baudry, C. M. Broadwell, J. H. Greenberg, R. R. Treacy, P. Cais, B. Quertier, P. Camino, A. Bos, and A. W. Gunst, "The ALMA correlator," *Astronomy and Astrophysics*, vol. 462, no. 2, pp. 801–810, 2007.

[22] R. H. Kingston, *Detection of optical and infrared radiation*, vol. 10. Springer-Verlag, 1978.

[23] C. H. Townes, "Spatial interferometry in the mid-infrared region," *Journal of Astrophysics and Astronomy*, vol. 5, no. 2, pp. 111–130, 1984.

[24] M. Teich, "Chapter 9 Coherent Detection in the Infrared," in *Semiconductors and Semimetals, Volume 5* (R. Willardson and A. C. Beer, eds.), pp. 361–407, Elseiver, 1970.

[25] D. Hale, M. Bester, W. Danchi, W. Fitelson, S. Hoss, E. Lipman, J. Monnier, P. Tuthill, and C. Townes, "The Berkeley Infrared Spatial Interferometer: A Heterodyne Stellar Interferometer for the Mid-Infrared," vol. 10, pp. 998–1012, 2000.

[26] S. Gulkis, "Thermal background Noise limitations," *TDA Progress Report*, no. September, pp. 53–59, 1982.

[27] E. Michael and F. Besser, "Breaking the heterodyne detection quantum noise limit with correlation," *IEEE Access(Submitted)*, 2017.

[28] M. J. Ireland and J. D. Monnier, "A Dispersed Heterodyne Design for the Planet Formation Imager (PFI)," p. 8, jul 2014.

[29] J. B. Ashcom, "White Light Heterodyne Interferometry SNR," no. April, 2015.

[30] F. Eisenhauer, W. Brandner, C. Straubmeier, K. Perraut, S. Gillessen, J. Lima, T. Henning, P. Garcia, S. Kellner, G. Avila, G. Perrin, W. Brandner, C. Straubmeier, K. Perraut, A. Amorim, M. Schöller, S. Gillessen, P. Kervella, M. Benisty, C. Araujo-Hauck, L. Jocou, J. Lima, G. Jakob, M. Haug, Y. Clénet, T. Henning, A. Eckart, J.-P. Berger, P. Garcia, R. Abuter, S. Kellner, T. Paumard, S. Hippler, S. Fischer, T. Moulin, J. Villate, G. Avila, A. Gräter, S. Lacour, A. Huber, M. Wiest, A. Nolot, P. Carvas, R. Dorn, O. Pfuhl, E. Gendron, S. Kendrew, S. Yazici, S. Anton, Y. Jung, M. Thiel, É. Choquet, R. Klein, P. Teixeira, P. Gitton, D. Moch, F. Vincent, N. Kudryavtseva, S. Ströbele, S. Sturm, P. Fédou, R. Lenzen, P. Jolley, C. Kister, V. Lapeyrère, V. Naranjo, C. Lucuix, R. Hofmann, F. Chapron, U. Neumann, L. Mehrgan, O. Hans, G. Rousset, J. Ramos, M. Suarez, R. Lederer, J.-M. Reess, R.-R. Rohloff, P. Haguenauer, H. Bartko, A. Sevin, K. Wagner, J.-L. Lizon, S. Rabien, C. Collin, G. Finger, R. Davies, D. Rouan, M. Wittkowski, K. Dodds-Eden, D. Ziegler, F. Cassaing, H. Bonnet, M. Casali, R. Genzel, and P. Lena, "GRAVITY: Observing the Universe in Motion," *The Messenger*, vol. 143, no. March, pp. 16–24, 2011.

[31] D. Pozar, *Microwave Engineering*. 2005.

[32] D. W. Allan, "Statistics of Atomic Frequency Standards," *Proceedings of the IEEE*, vol. 54, no. 2, pp. 221–230, 1966.

[33] J. A. Barnes, A. R. Chi, L. S. Cutler, D. J. Healey, D. B. Leeson, T. E. McGunigal, J. A. Mullen, W. L. Smith, R. L. Sydnor, R. F. C. Vessot, and G. M. R. Winkler, "Characterization of Frequency Stability," *IEEE Transactions on Instrumentation and Measurement*, vol. IM-20, pp. 105–120, may 1971.

[34] R. Schieder, G. Rau, and B. Vowinkel, "Characterization and Measurement of System Stability," in *Instrumentation for Submillimeter Spectroscopy* (E. L. Kollberg, ed.), vol. 598, pp. 189–192, apr 1986.

[35] W. J. Riley, *Handbook of Frequency Stability Analysis*, vol. 31. 2008.

[36] L. Pallanca, C. Vio, and E. Michael, "A low-cost fiber-based near-infrared heterodyne interferometer," *SPIE . . .*, 2012.

[37] *Balanced Photoreceivers*. No. 408, New Focus.

[38] Casper, "ROACH." `https://casper.berkeley.edu/wiki/ROACH`.

[39] Casper, "ROACH FPGA Interfaces." https://casper.berkeley.edu/wiki/ROACH_FPGA_Interfaces.

[40] *5007 Dual Synthesizer Configuration Manager User ' s Guide (admin Version)*.

[41] "Fiber-coupled Acousto-Optic Frequency Shifters." https://www.brimrose.com/fiber-coupled-frequency-shifters.